NASA Contractor Report 165611

DEVELOPMENT OF A SPINNING WAVE HEAT ENGINE

By
B. T. Zinn, E. A. Powell and J. E. Hubbartt

Prepared for
NATIONAL AERONAUTICS AND SPACE ADMINISTRATION
Lewis Research Center

Under
Grant NAG3-96

August 1982

GEORGIA INSTITUTE OF TECHNOLOGY
A UNIT OF THE UNIVERSITY SYSTEM OF GEORGIA
SCHOOL OF AEROSPACE ENGINEERING
ATLANTA, GEORGIA 30332

NASA Contractor Report 165611

DEVELOPMENT OF A SPINNING WAVE HEAT ENGINE

B. T. Zinn, E. A. Powell and J. E. Hubbartt

Georgia Institute of Technology
School of Aerospace Engineering
Atlanta, Georgia 30332

August 1982

Prepared for

NATIONAL AERONAUTICS AND SPACE ADMINISTRATION
Lewis Research Center
Under Grant NAG3-96

FOREWORD

The research described herein, which was conducted at Georgia Institute of Technology, was supported by NASA Grant No. NAG 3-96. The work was done under the management of the NASA Project Manager, Bert R. Phillips, Wind and Stationary Power Division, NASA-Lewis Research Center.

ABSTRACT

A theoretical analysis and an experimental investigation were conducted to assess the feasibility of developing a spinning wave heat engine. Such an engine would utilize a large amplitude traveling acoustic wave rotating around a cylindrical chamber, and it should not suffer from the inefficiency, noise, and intermittent thrust which characterizes pulse jet engines. The objective of this investigation was to determine whether an artificially driven large amplitude spinning transverse wave could induce a steady flow of air through the combustion chamber under cold flow conditions. In the theoretical analysis the Maslen and Moore perturbation technique was extended to study flat cylinders (pancake geometry) with completely open side walls and a central opening. In the parallel experimental study, a test model was used to determine resonant frequencies and radial pressure distributions, as well as oscillatory and steady flow velocities at the inner and outer peripheries. The experimental frequency was nearly the same as the theoretical acoustic value for a model of the same outer diameter but without a central hole. Although the theoretical analysis did not predict a steady velocity component, simultaneous measurements of hotwire and microphone responses have shown that the spinning wave pumps a mean flow radially outward through the cavity. This conclusion has been verified by flow visualization using both a sensitive tufted wand and smoke as flow tracers. These results indicate that further development and testing of the spinning wave engine concept is warranted.

TABLE OF CONTENTS

INTRODUCTION

This report is a summary of work conducted under NASA Grant No. NAG3-96 during the period September 8, 1980 through September 7, 1981. This project is entitled "Development of a Spinning Wave Heat Engine" and the NASA Technical Officer is B. R. Phillips at the Lewis Research Center.

The purpose of this research program is to provide basic information needed for the development of a spinning wave heat engine originally conceived by M. F. Heidmann at the NASA Lewis Research Center. The spinning wave heat engine concept is based on the presence of a large amplitude traveling acoustic wave rotating around a cylindrical chamber. The spinning wave engine is conceptually similar to the pulse jet engine, but fundamental differences between the two engines suggest that the spinning wave concept can eliminate or alleviate the problems of inefficiency, noise, and intermittent thrust that caused the demise of pulse jet engine development. On the other hand, the spinning wave engine retains the characteristics of simplicity, low cost, low weight and absence of rotating parts that stimulated the development of pulse jets in the early 1950's.

As a propulsive unit by itself, a spinning wave engine is not a competitor of current engines for commercial CTOL and V/STOL aircraft. Effective pressure ratio is relatively low (less than 5:1) and, therefore, specific fuel consumption for such applications would be relatively high. The concept, however, remains attractive for many applications such as military, powered glides, auxiliary power, precompression stage for other engine cycles, and ground-effect vehicles. Within its pressure ratio range, the cycle efficiency of a spinning wave engine can be higher than that of other cycles because heat is essentially added at constant volume.

In order for the spinning wave engine to function, the spinning acoustic wave must induce a steady flow of air through the combustion chamber. Such a steady flow is a property of nonlinear waves (i.e., large amplitude) in which the oscillating flow in one direction is greater than that in the opposite direction and a net through flow results. In the nonlinear analysis by Maslen and Moore[1], large amplitude standing and traveling acoustic waves in a closed circular cylinder were studied using a perturbation technique. Maslen and Moore's results indicate that a small depression of mean pressure occurs at the center and a small elevation of mean pressure occurs at the periphery when a large amplitude traveling first tangential (1T) wave is present. However, no net through flow can occur for this geometry because there are no inlet and outlet openings. When viscosity is included in the analysis, a steady wheel flow is predicted which rotates in a direction opposite to the direction of wave travel for low order modes. This wheel flow, however, does not contribute to a net flow through the chamber.

In order to obtain a steady flow through the combustor, an inlet and outlet must be provided. The results of Maslen and Moore for the spinning 1T mode appear to imply that if openings are provided at the center and at the periphery of the cylinder, a net inflow will occur at the center and an outflow will occur at the periphery. Providing the openings, however, will modify the boundary conditions at the center and the periphery so that Maslen and Moore's analysis no longer applies. In the most extreme case the side wall of the cylinder is completely open and the boundary condition at the wall requires (approximately) that the pressure oscillations vanish there (in contrast to the closed cylinder in which the radial velocity component vanishes at the wall). Similarly, providing a central inlet is expected to modify the structure of the spinning transverse modes.

In this investigation the acoustic generation of a steady through flow in the absence of combustion is determined by extending the Maslen and Moore analysis to include the effects of inlet and outlet openings. This work is divided into two parts. In the first part the Maslen and Moore technique is used to study flat cylinders (pancake geometry) with completely open side walls and a central opening. In the second part an experimental apparatus is used to verify the analytical results. The remainder of this report summarizes the analytical and experimental work done under this project.

THEORETICAL ANALYSIS

The objective of the theoretical analysis described herein is to determine whether a large amplitude spinning acoustic wave can pump a steady flow through a flat cylindrical chamber which is open on the periphery and at the center. Such an annular pancake cavity is formed by two parallel, closely spaced annular disks as shown in Figure 1. To minimize losses due to acoustic radiation and to ensure a two-dimensional acoustic solution, the spacing h between the disks must be small compared to the outer radius b; that is $h/b << 1$. Under these conditions the pressure at the open boundaries is approximately equal to the ambient pressure; that is, as a first approximation the pressure perturbation must vanish at the outer edge ($r^* = b$) and inner edge ($r^* = a$) of the annular plates. This is analogous to the open-end boundary condition used in the analysis of organ pipes. In contrast, the nonlinear analysis of Maslen and Moore(1) was applied to hard walled cylinders for which the radial velocity component must vanish at the outer boundary (there is no inner boundary in this case). In fact for the first tangential spinning mode, the maximum pressure fluctuation occurs at the hard walled boundary in the Maslen and Moore analysis.

Although the boundary conditions are different, the governing differential equations are the same for both geometries. Therefore the approach taken in this analysis is to follow closely the Maslen and Moore procedure, substituting the appropriate boundary conditions where necessary. This leads to some serious difficulties, which have not been satisfactorily resolved. Nevertheless it is believed that the solutions obtained in this manner are instructive and shed some light on the expected

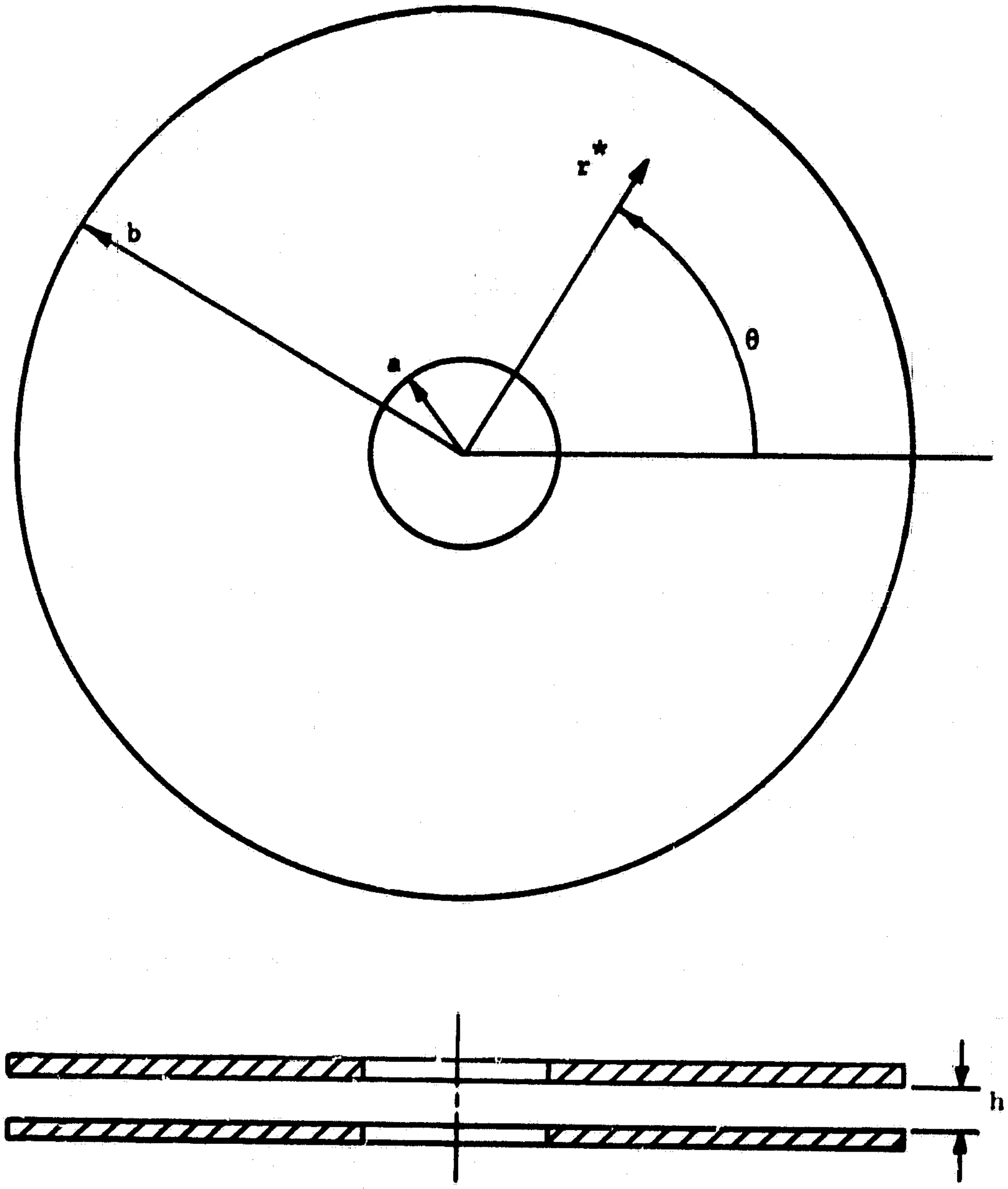

Figure 1. Annular Pancake Geometry and Coordinate System.

behavior of the spinning wave engine. The exploration of alternative methods of analysis, such as the Method of Weighted Residuals,(2,3,4) was beyond the scope of this one-year project.

Modification of Maslen and Moore Analysis

Basic Procedure. In the Maslen and Moore analysis it is assumed that the flow is isentropic and irrotational so that a velocity potential, φ, exists such that $\nabla\varphi = \underset{\rightarrow}{u}$. The energy and state equations yield the isentropic flow relation, $P = \rho^{\gamma}$. The continuity and momentum equations yield the following equation for the velocity potential:

$$\nabla^2\varphi - \varphi_{tt} = 2\nabla\varphi \cdot \nabla\varphi_t + \frac{\gamma-1}{2}(\nabla\varphi \cdot \nabla\varphi)\,\nabla^2\varphi + \frac{1}{2}\,\nabla\varphi \cdot \nabla(\nabla\varphi \cdot \nabla\varphi)$$

$$+ (\gamma-1)\,\varphi_t\,\nabla^2\varphi \qquad (1)$$

where γ is the specific heat ratio and the pressure is related to φ by:

$$1 - P^{\frac{\gamma-1}{\gamma}} = (\gamma-1)\left[\varphi_t + \frac{1}{2}\,\nabla\varphi \cdot \nabla\varphi\right] \qquad (2)$$

The above equations involve only dimensionless quantities defined as follows:

P = nondimensional pressure, P^*/P_o

t = nondimensional time, ωt^*

u,v,w = nondimensional axial, radial, and tangential velocities (cylindrical coordinates), u^*/c_o, v^*/c_o, w^*/c_o

$\underset{\rightarrow}{u}$ = nondimensional velocity vector, $\underset{\rightarrow}{u}^*/c_o$

x = nondimensional axial coordinate, $\omega x^*/c_o$

α = nondimensional radial coordinate, $\omega r^*/c_o$

θ = angle in cylindrical coordinates

ρ = nondimensional density, ρ^*/ρ_o

where ω is the angular frequency (dimensional), c_o is the velocity of sound in the absence of the wave, the subscript o refers to dimensional flow properties in the absence of the wave, and the superscript* refers to dimensional properties.

In the perturbation procedure used by Maslen and Moore the velocity potential and pressure are expanded in terms of an amplitude parameter ϵ, thus

$$\varphi = \epsilon\varphi^{(1)} + \epsilon^2\varphi^{(2)} + \epsilon^3\varphi^{(3)} + \dots \qquad (3)$$

and

$$P = 1 + \epsilon P^{(1)} + \epsilon^2 P^{(2)} + \epsilon^3 P^{(3)} + \dots \qquad (4)$$

Substituting Eqs. (3) and (4) into Eqs. (1) and (2), collecting and grouping terms according to powers of ϵ, and equating the resulting coefficients of each power of ϵ to zero gives equations to be solved successively for the first, second and third order potentials and pressures.

<u>First Order Solutions</u>. Equating the coefficient of ϵ in Eq. (1) to zero gives the wave equation for the first order potential $\varphi^{(1)}$:

$$\nabla^2\varphi^{(1)} - \varphi^{(1)}_{tt} = 0 \qquad (5)$$

while Eq. (2) yields:

$$P^{(1)} = -\gamma\varphi^{(1)}_t \qquad (6)$$

Spinning wave solutions of Eq. (5) were obtained by the method of separation of variables and were required to satisfy the boundary conditions $p^{(1)} = 0$ at $r^* = a$ (inner) and $r^* = b$ (outer) boundaries. These acoustic solutions for the velocity potential $\varphi^{(1)}$ have the form:

$$\varphi^{(1)} = \left\{ J_n\left(\beta_{nk} r\right) - \left[\frac{J_n(\nu\beta_{nk})}{Y_n(\nu\beta_{nk})}\right] Y_n(\beta_{nk} r)\right\} \sin(t + n\theta) \quad (7)$$

where J_n and Y_n are Bessel functions of the first and second kinds, respectively, of order n. The parameter ν is the ratio of inner radius to outer radius, $\nu = a/b$, and the eigenvalue β_{nk} is the k^{th} solution of the equation

$$J_n(x)Y_n(\nu x) - Y_n(x)J_n(\nu x) = 0. \quad (8)$$

The velocity potential $\varphi^{(1)}$ is expressed in terms of the dimensionless radius $r = r^*/b$, the angular coordinate θ, and the dimensionless time t. The actual frequency f is then related to the eigenvalue by

$$f = \frac{c_o}{2\pi b} \beta_{nk} \quad (9)$$

The acoustic pressure is then given by

$$p^{(1)} = -\gamma R_n(\alpha) \cos(t + n\theta) \quad (10)$$

where $R_n(\alpha)$ is the radial acoustic eigenfunction given by

$$R_n(\alpha) = J_n(\alpha) - \frac{J_n(\nu\beta_{nk})}{Y_n(\nu\beta_{nk})} Y_n(\alpha) \tag{11}$$

and $\alpha = \omega r^*/c_o = \beta_{nk} r^*/b = \beta_{nk} r$.

Detailed calculations of the radial eigenfunctions, eigenvalues and pressure fields have been carried out for the principal mode of interest, the spinning first tangential mode ($n = 1, k = 1$). A plot of the eigenvalue β_{11} as a function of ν is shown in Figure 2, which implies that the frequency increases as the diameter of the central opening increases. For $\nu < 0.1$ Figure 2 also shows that the frequency is close to the value ($\beta_{11} = 3.83171$) obtained when no central opening is present (i.e., two closely spaced disks). The radial dependence of $\varphi^{(1)}$ is shown in Figure 3 for $\nu = 0$, 0.1, and 0.2. For the case of no central opening ($\nu = 0$) the coefficient of Y_1 vanishes ($Y_1(0) = -\infty$) and the solution becomes $\varphi^{(1)} = J_1(\beta_{11} r) \sin(t + \theta)$. Figure 4 shows the pressure field (isobars) for the case $\nu = 0$ (no central opening), while Figure 5 shows isobars for $\nu = 0.2$.

<u>Second Order Solutions</u>. Setting the coefficient of ϵ^2 in Eq. (1) equal to zero yields the following equation for the second order potential $\varphi^{(2)}$

$$\nabla^2 \varphi^{(2)} - \varphi^{(2)}_{tt} = \Big[\nabla\varphi^{(1)} \cdot \nabla\varphi^{(1)} + \frac{\gamma-1}{2} \Big(\varphi^{(1)}_t\Big)\Big]^2_t \tag{12}$$

ORIGINAL PAGE IS
OF POOR QUALITY

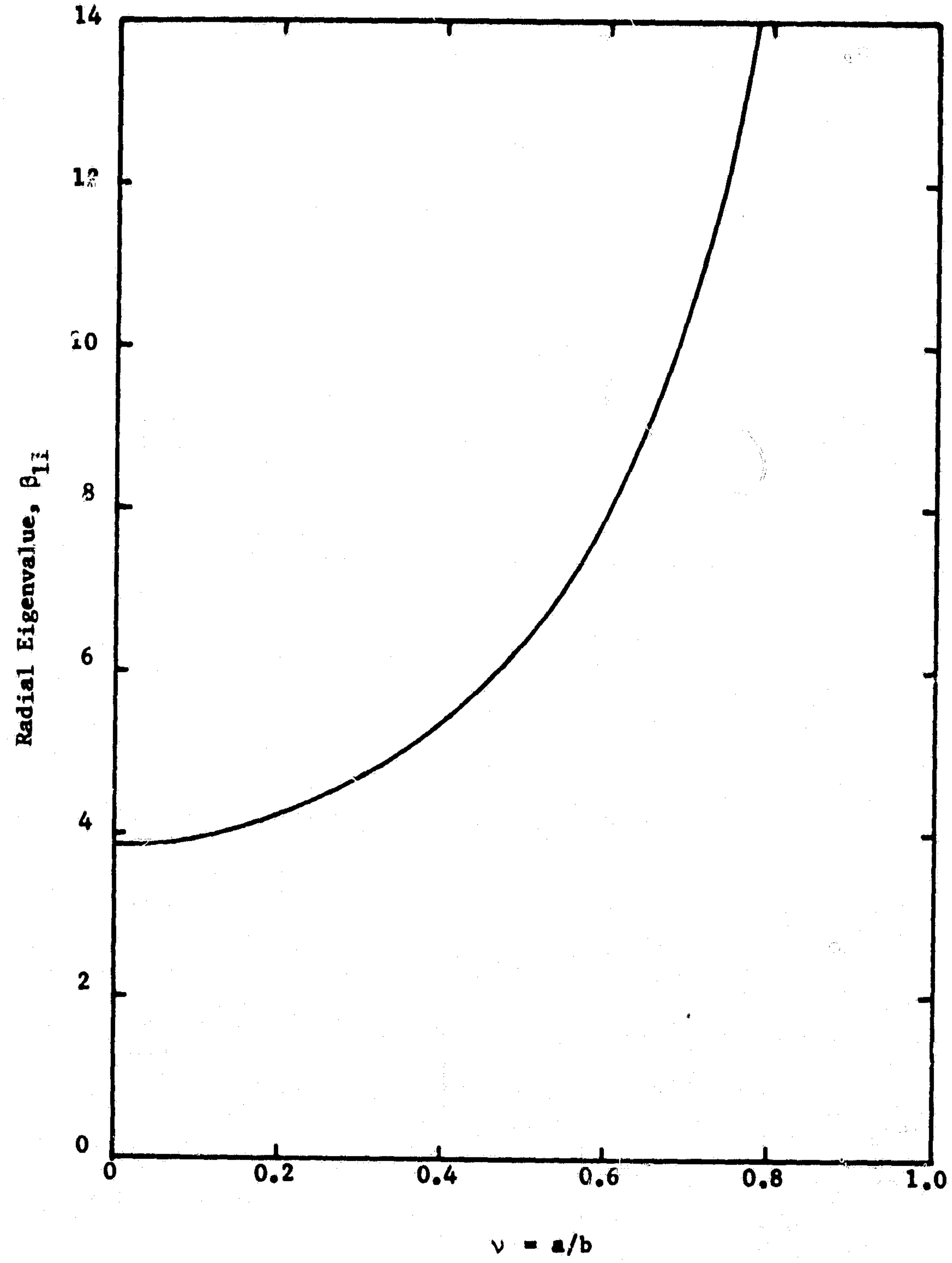

Figure 2. Radial Eigenvalues for Open Annuli for n = 1.

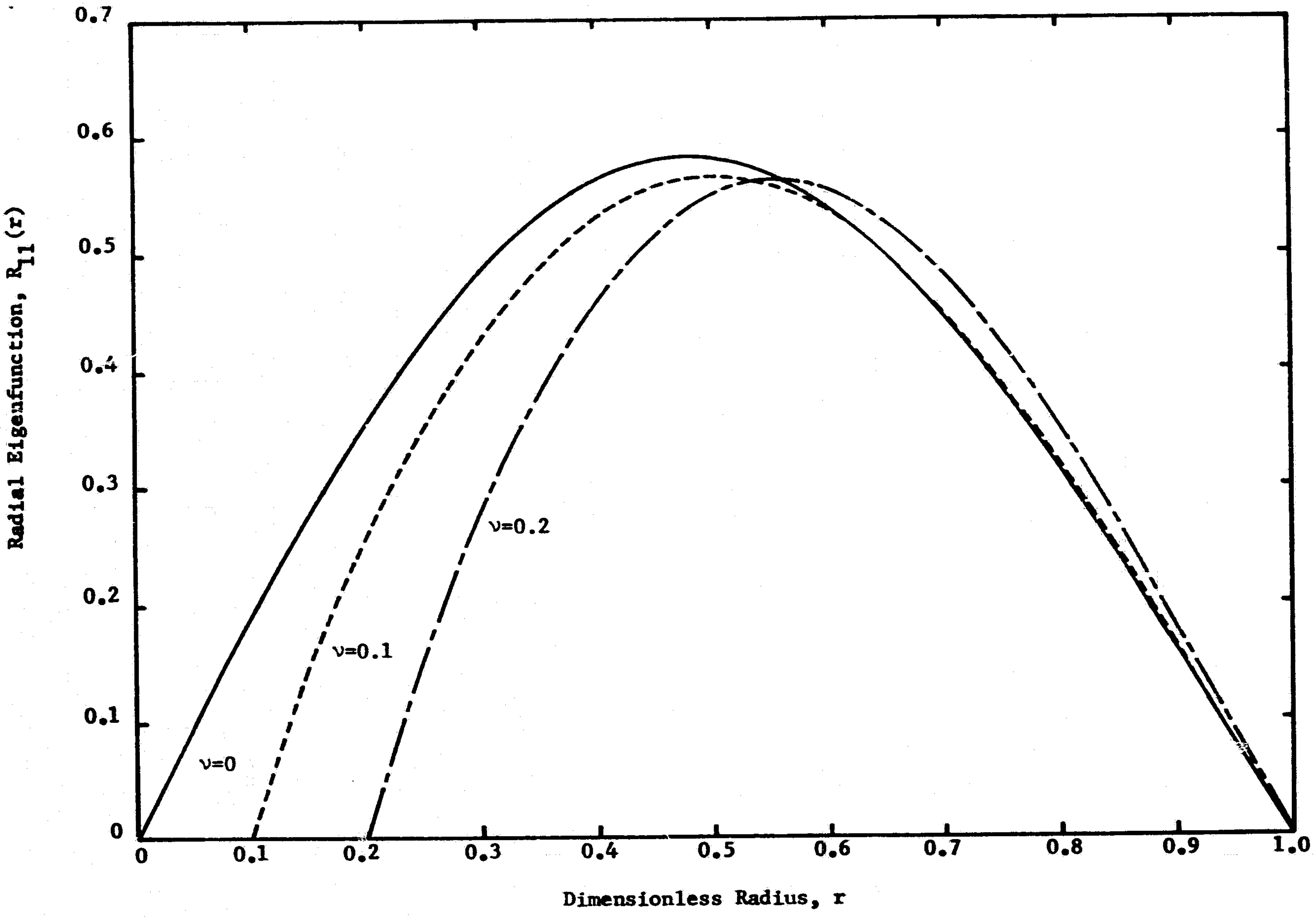

Figure 3. Radial Eigenfunctions for Open Annuli for n = 1.

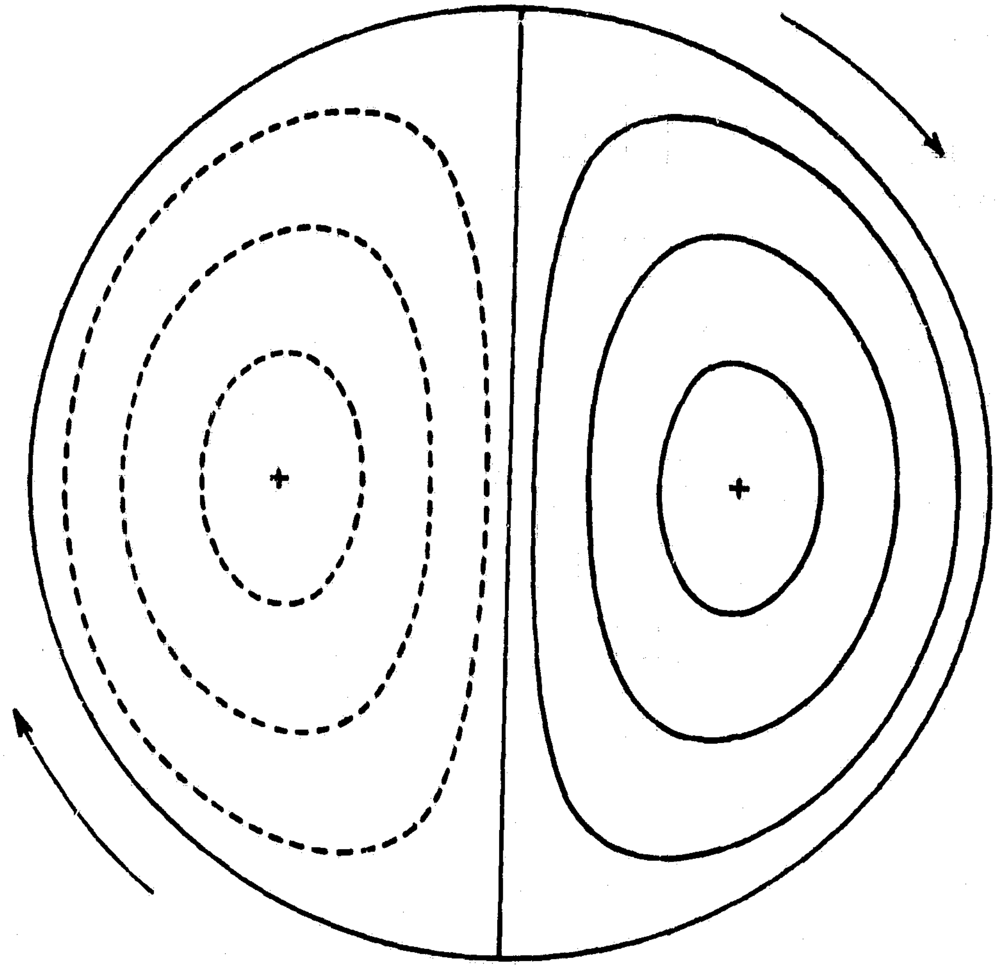

Figure 4. Isobars for Open Pancake Geometry with No Central Opening for Spinning 1T Mode.

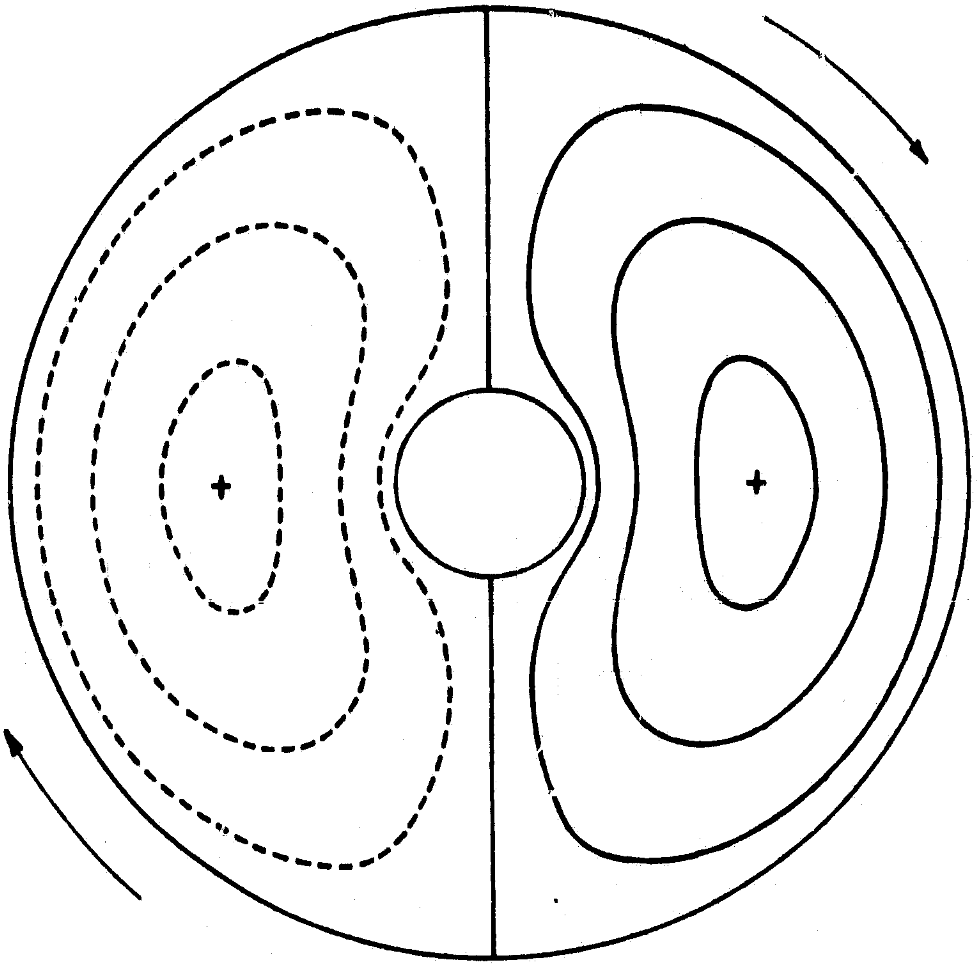

Figure 5. Isobars for Open Annulus with $\nu = 0.2$ for Spinning 1T Mode.

where only the known first order solutions appear on the right hand side. Following Maslen and Moore, Eq. (12) is assumed to have a solution of the form

$$\varphi^{(2)} = \frac{1}{2} \sin 2(t + n\theta) \left[R_n^2(\alpha) - (\gamma + 1) f(\alpha)\right] \qquad (13)$$

Substituting Eq. (13) into the left-hand-side of Eq. (12) and the first order solution given by Eq. (7) into the right-hand-side of Eq. (12) yields the following inhomogeneous Bessel equation for $f(\alpha)$:

$$f''(\alpha) + \frac{1}{\alpha} f'(\alpha) + 4\left(1 - \frac{n^2}{\alpha^2}\right) f(\alpha) = R_n^2(\alpha) \qquad (14)$$

where the primes indicate differentiation with respect to α.

Equating the coefficient of ϵ^2 in Eq. (2) to zero gives the following relation for $P^{(2)}$ in terms of the first and second order potentials $\varphi^{(1)}$ and $\varphi^{(2)}$:

$$P^{(2)} = -\gamma\left[\varphi_t^{(2)} + \frac{1}{2} \nabla\varphi^{(1)} \cdot \nabla\varphi^{(1)} - \frac{1}{2}\left(\varphi_t^{(1)}\right)^2\right] \qquad (15)$$

Substituting the first and second order potentials (i.e. Eqs. (7) and (13)) into Eq. (15) gives the solution for $P^{(2)}$ as:

$$P^{(2)} = -\gamma\left[P_{20}(\alpha)\cos 2(t + n\theta) + P_{23}(\alpha)\right] \qquad (16)$$

where

$$P_{20}(\alpha) = \frac{1}{4}\left(3 + \frac{n^2}{\alpha^2}\right) R_n^2(\alpha) - \frac{1}{4}\left[R_n'(\alpha)\right]^2 - (\gamma + 1) f(\alpha) \qquad (17)$$

and $$P_{23}(\alpha) = \frac{1}{4}\left[R_n'(\alpha)\right]^2 - \frac{1}{4}R_n^2(\alpha)\left(1 - \frac{n^2}{\alpha^2}\right) \qquad (18)$$

The second order contribution to the pressure is thus seen to consist of a double frequency component (i.e., $P_{20}(\alpha)\cos 2(t + n\theta)$) and a steady component (i.e., $P_{23}(\alpha)$).

In order to complete the second order solutions, the function $f(\alpha)$ must be obtained by solving Eq. (14). Since this is a second order differential equation, the solution for $f(\alpha)$ will contain two arbitrary constants. These constants must be obtained by imposing the boundary conditions at the inner and outer radii; namely, that the pressure perturbations vanish there. This is not as straightforward as it at first might seem, because the relationship between the dimensionless radial coordinate α and the dimensional radial coordinate r^* involves the angular frequency ω. Since the frequency is usually dependent upon amplitude for nonlinear systems, the application of the boundary conditions becomes complicated. Therefore the determination of the frequency dependence upon amplitude and the application of the boundary conditions will be deferred until after the third order solutions have been derived. The solution for $f(\alpha)$ is given in Appendix A.

<u>Third Order Solutions</u>. Equating the coefficient of ϵ^3 in Eq. (1) to zero yields the following equation governing the third order potential φ^3:

$$\nabla^2\varphi^{(3)} - \varphi_{tt}^{(3)} = \frac{1}{2}\nabla\varphi^{(1)}\cdot\nabla\left(\nabla\varphi^{(1)}\cdot\nabla\varphi^{(1)}\right) - \frac{\gamma-1}{2}\nabla\varphi^{(1)}\cdot\nabla\varphi^{(1)}\varphi_{tt}^{(1)} +$$

$$+ (\gamma-1)^2 \varphi_t^{(1)} \varphi_t^{(1)} \varphi_{tt}^{(1)} + \Big[2 \nabla\varphi^{(1)} \cdot \nabla\varphi^{(2)} +$$

$$+ (\gamma-1) \varphi_t^{(1)} \varphi_t^{(2)} + (\gamma-1) \nabla\varphi^{(1)} \cdot \nabla\varphi^{(1)} \varphi_t^{(1)} \Big]_t \qquad (19)$$

where only the known first and second order solutions appear on the right hand side. As in the Maslen and Moore analysis, this equation is assumed to have a solution of the form:

$$\varphi^{(3)} = F_1(\alpha) \sin 3 (t + n\theta) + F_5(\alpha) \sin (t + n\theta) \qquad (20)$$

where the functions $F_1(\alpha)$ and $F_5(\alpha)$ satisfy the following inhomogeneous Bessel equations:

$$F_1'' + \frac{1}{\alpha} F_1' + 9 \left(1 - \frac{n^2}{\alpha^2}\right) F_1 = \mathcal{R}_1(\alpha) \qquad (21)$$

$$F_5'' + \frac{1}{\alpha} F_5' + \left(1 - \frac{n^2}{\alpha^2}\right) F_5 = \mathcal{R}_5(\alpha) \qquad (22)$$

The inhomogeneous terms $\mathcal{R}_1(\alpha)$ and $\mathcal{R}_5(\alpha)$ appearing in Eqs. (21) and (22) are determined by substituting the first and second order potentials (i.e., Eqs. (7) and (13)) into Eq. (19), and they are given in Appendix B.

Also the third order pressure contribution $P^{(3)}$ was derived by applying the perturbation analysis to the nonlinear relation between pressure and velocity potential (Eq. (12)) to obtain:

$$P^{(3)} = -\gamma\left[\varphi_t^{(3)} + \nabla\varphi^{(1)} \cdot \nabla\varphi^{(2)} - \varphi_t^{(1)}\varphi_t^{(2)} - \frac{1}{2}\varphi_t^{(1)}\,\nabla\varphi^{(1)} \cdot \nabla\varphi^{(1)} + \frac{2-\gamma}{6}\left(\varphi_t^{(1)}\right)^3\right] \tag{23}$$

Substituting the first, second, and third order potentials into Eq. (23) gives the solution for $P^{(3)}$ as:

$$P^{(3)} = -\gamma P_{30} \cos 3(t + n\theta) - \gamma P_{34} \cos(t + n\theta) \tag{24}$$

where

$$P_{30}(\alpha) = 3F_1 + \left(\frac{\gamma+1}{4}\right)R_n' f' + \left(\frac{\gamma+1}{2}\right)\left(1 - \frac{n^2}{\alpha^2}\right)R_n f + \frac{R_n}{8}\left\{-3(R_n')^2 + \left[3\frac{n^2}{\alpha^2} - \frac{\gamma+10}{3}\right]R_n^2\right\} \tag{25}$$

$$P_{34}(\alpha) = F_5 - \left(\frac{\gamma+1}{4}\right)R_n' f' + \left(\frac{\gamma+1}{2}\right)\left(1 - \frac{n^2}{\alpha^2}\right)R_n f + \frac{R_n}{8}\left\{3(R_n')^2 + \left[\frac{n^2}{\alpha^2} - (\gamma+2)\right]R_n^2\right\} \tag{26}$$

The third order contribution to the pressure is thus seen to consist of a third harmonic component (i.e., $P_{30} \cos 3(t + n\theta)$) and a correction to the fundamental (i.e., $P_{34} \cos(t + n\theta)$).

In order to complete the third order solutions the radial functions $F_1(\alpha)$ and $F_5(\alpha)$ must be obtained by solving Eqs. (21) and (22) subject to the boundary conditions applied at the inner and outer radii. This depends on the amplitude dependence of the frequency which will be considered in the next section. The solutions for $F_1(\alpha)$ and $F_5(\alpha)$ are given in Appendix B.

In both the second and third order solutions, the expressions for $\varphi^{(2)}$, $\varphi^{(3)}$, $P_{20}(\alpha)$, $P_{23}(\alpha)$, $P_{30}(\alpha)$, and $P_{34}(\alpha)$ as well as the differential equations governing $f(\alpha)$, $F_1(\alpha)$ and $F_5(\alpha)$ agree with their counterparts in the original Maslen and Moore analysis if one replaces $R_n(\alpha)$ with $J_n(\alpha)$.

Boundary Conditions and Dependence of Frequency Upon Amplitude. The perturbation technique of Maslen and Moore also requires that the frequency varies with amplitude according to the expansion

$$\omega = \omega_0 + \epsilon\omega_1 + \epsilon^2\omega_2 + \epsilon^3\omega_3 + \dots \tag{27}$$

where ω_0 is the acoustic frequency. This is equivalent to expanding the eigenvalue $\beta = b\omega/c_0$, thus

$$\beta = \beta_0 + \epsilon\beta_1 + \epsilon^2\beta_2 + \epsilon^3\beta_3 + \dots \tag{28}$$

In the remaining discussions the subscripts denoting the tangential and radial mode numbers n and k for the eigenvalue β_{nk} will be dropped.

In order to determine the coefficients β_1, β_2, ... in Eq. (28), the pressure was required to satisfy the boundary condition $P - 1 = 0$ at the outer radius $\alpha = \beta$ and at the inner radius $\alpha = \nu\beta$, thus

$$\epsilon P^{(1)}(\beta,\theta,t) + \epsilon^2 P^{(2)}(\beta,\theta,t) + \epsilon^3 P^{(3)}(\beta,\theta,t) = 0 \qquad (29a)$$

$$\epsilon P^{(1)}(\nu\beta,\theta,t) + \epsilon^2 P^{(2)}(\nu\beta,\theta,t) + \epsilon^3 P^{(3)}(\nu\beta,\theta,t) = 0 \qquad (29b)$$

Substituting the expansion of β given by Eq. (28) into Eqs. (29), expanding each term in a Taylor series about the acoustic value β_o or $\nu\beta_o$, and equating the coefficients of each power of ϵ to zero yield the boundary conditions for the second order function $f(\alpha)$ and the third order functions $F_1(\alpha)$ and $F_5(\alpha)$.

In particular, equating the coefficient of ϵ to zero yields $R_n(\beta_o) = R_n(\nu\beta_o) = 0$ which is already satisfied from the definition of β_o.

From the coefficient of ϵ^2 one obtains the following expressions:

$$\beta_1 R_n'(\beta_o) \cos(t + n\theta) + P_{20}(\beta_o) \cos 2(t + n\theta) + P_{23}(\beta_o) = 0 \qquad (30a)$$

$$\nu\beta_1 R_n'(\nu\beta_o) \cos(t + n\theta) + P_{20}(\nu\beta_o) \cos 2(t + n\theta) + P_{23}(\nu\beta_o) = 0 \qquad (30b)$$

Equations (30) must be satisfied for all values of t and θ, thus each term must separately vanish. The first term is zero only if β_1 vanishes, since the derivatives of the eigenfunctions $R_n'(\beta_o)$ and $R_n'(\nu\beta_o)$ are not zero at the boundaries (see Figure 3). The other two terms require that the second order pressure functions $P_{20}(\alpha)$ and $P_{23}(\alpha)$ vanish at $\alpha = \nu\beta_o$ and $\alpha = \beta_o$. Thus the first order correction to the eigenvalue β_1 is zero which agrees with the well-known result from linear acoustics that the frequency is independent of amplitude. From Eq. (17) the boundary conditions on $P_{20}(\alpha)$ yield the following boundary conditions to be satisfied by the second order function $f(\alpha)$:

$$f(\beta_o) = \frac{-1}{4(\gamma+1)}\left[R_n'(\beta_o)\right]^2 \tag{31a}$$

$$f(\nu\beta_o) = \frac{-1}{4(\gamma+1)}\left[R_n'(\nu\beta_o)\right]^2 \tag{31b}$$

On the other hand, Eq. (18) and the boundary conditions on $P_{23}(\alpha)$ require that $R_n'(\beta_o)$ and $R_n'(\nu\beta_o)$ vanish, which is impossible since the derivatives of the eigenfunctions R_n are finite at the boundaries. This implies that the condition that the pressure perturbation vanish at the inner and outer boundaries cannot be satisfied in the framework of the Maslen and Moore theory.

The failure of the second order solutions to satisfy the boundary conditions is the difficulty mentioned previously. This residual pressure perturbation (P - 1), which is independent of time and angle, is given to second order by (using Eqs. (29), (16) and (18)):

$$P'(\beta_o) = \frac{-\gamma\epsilon^2}{4}\left[R_n'(\beta_o)\right]^2 \tag{32a}$$

$$P'(\nu\beta_o) = \frac{-\gamma\epsilon^2}{4}\left[R_n'(\nu\beta_o)\right]^2 \tag{32b}$$

where P' is the dimensionless pressure perturbation $P-1$. These boundary residuals appear to arise from the nonlinear terms in the relationship between pressure and velocity potential (i.e., Eq. (2)). It is possible that these boundary residuals are an inherent error associated with the Maslen and Moore analysis when one attempts to satisfy pressure boundary conditions with a perturbation analysis based on a velocity potential. In the original Maslen and Moore analysis for a cylinder with rigid boundaries, one required the normal velocity component to vanish at the boundary. Since the velocity is linearly related to the velocity potential, the boundary residuals did not appear in the original analysis. Further analysis of this problem has not yielded a method of satisfying the pressure boundary conditions to second order. Therefore the approach to be taken in the remainder of the analysis will be to accept these boundary residuals as part of the error incurred by using an approximate perturbation analysis.

Returning to the Taylor series expansion of Eqs. (29), setting the coefficients of ϵ^3 equal to zero yields:

$$\left[\beta_2 R_n'(\beta_o) + P_{34}(\beta_o)\right] \cos(t + n\theta) + P_{30}(\beta_o) \cos 3(t + n\theta) = 0 \qquad (33a)$$

$$\left[\nu\beta_2 R_n'(\nu\beta_o) + P_{34}(\nu\beta_o)\right] \cos(t + n\theta) + P_{30}(\nu\beta_o) \cos 3(t + n\theta) = 0 \qquad (33b)$$

where $\beta_1 = 0$ has been used. Again each term must vanish separately. The second term, along with Eq. (25), yields the following boundary conditions to be satisfied by $F_1(\alpha)$:

$$F_1(\beta_o) = \frac{-(\gamma+1)}{12} R_n'(\beta_o) f(\beta_o) \qquad (34a)$$

$$F_1(\nu\beta_o) = \frac{-(\gamma+1)}{12} R_n'(\nu\beta_o) f'(\nu\beta_o) \tag{34b}$$

The first term and Eq. (26) give the boundary conditions for $F_5(\alpha)$ in terms of the second order correction to the eigenvalue β_2 as follows:

$$F_5(\beta_o) = \frac{\gamma+1}{4} R_n'(\beta_o) f'(\beta_o) - \beta_2 R_n'(\beta_o) \tag{35a}$$

$$F_5(\nu\beta_o) = \frac{\gamma+1}{4} R_n'(\nu\beta_o) f'(\nu\beta_o) - \nu\beta_2 R_n'(\nu\beta_o) \tag{35b}$$

The eigenvalue correction β_2 can only be obtained after the inhomogeneous Bessel equation for $F_5(\alpha)$ (i.e., Eq. (22)) has been solved. This analysis is given in Appendix B and yields the following expression for β_2:

$$\beta_2 = \frac{\frac{\gamma+1}{4}\left[R_n'(\beta_o) f'(\beta_o) - \sigma R_n'(\nu\beta_o) f'(\nu\beta_o)\right] - F_{5p}(\beta_o)}{R_n'(\beta_o) - \nu\sigma R_n'(\nu\beta_o)} \tag{36}$$

where $\sigma = J_n(\beta_o)/J_n(\nu\beta_o)$ and $F_{5p}(\alpha)$ is the particular solution of Eq. (22) given in Appendix B.

Total Solutions. In order to obtain numerical solutions relevant to the spinning wave engine, expressions for combining the first, second, and third order solutions given in the preceding sections are needed. These are based on the expansions of the velocity potential and pressure given by Eqs. (3) and (4) where the dependence of frequency upon amplitude is accounted for by the Taylor series expansion procedure used in the previous section. Since we are interested in interior points as well as boundary points, the Taylor expansion is performed about $\alpha_o = \beta_o r$ where $\alpha = (\beta_o + \epsilon^2 \beta_2)r$.

The pressure perturbation P' is thus obtained from Eq. (4) using a Taylor expansion about $\beta_o r$ to give:

$$P'(r,\theta,t) = \epsilon P^{(1)}(\beta_o r,\theta,t) + \epsilon^2 P^{(2)}(\beta_o r,\theta,t)$$

$$+ \epsilon^3 \left\{ P^{(3)}(\beta_o r,\theta,t) + \beta_2 r \frac{\partial P^{(1)}}{\partial \alpha}(\beta_o r,\theta,t) \right\} \qquad (37)$$

Using Eqs. (10), (16), and (24) in Eq. (37) yields

$$P = -\gamma \left\{ \epsilon^2 P_{23}(\alpha) + \left[\epsilon R_n(\alpha) + \epsilon^3 P_{34}(\alpha) + \epsilon^3 \alpha \zeta_2 R_n'(\alpha) \right] \cos(t+n\theta) \right.$$

$$\left. + \epsilon^2 P_{20}(\alpha) \cos 2(t+n\theta) + \epsilon^3 P_{30}(\alpha) \cos 3(t+n\theta) \right\} \qquad (38)$$

where $\zeta_2 = \beta_2/\beta_o$ and computations are made using the acoustic eigenvalue β_o in determining α (i.e., using $\alpha = \beta_o r$ in Eq. (38)).

The acoustic velocity components are also of considerable interest in the spinning wave engine analysis, since they are needed to determine the acoustic pumping of a steady flow through the engine. The radial velocity v and tangential velocity w are determined from the definition of the velocity potential and Eq. (3) as follows:

$$v = \frac{\partial \varphi}{\partial \alpha} = \epsilon \frac{\partial \varphi^{(1)}}{\partial \alpha} + \epsilon^2 \frac{\partial \varphi^{(2)}}{\partial \alpha} + \epsilon^3 \frac{\partial \varphi^{(3)}}{\partial \alpha} \qquad (39)$$

$$w = \frac{1}{\alpha} \frac{\partial \varphi}{\partial \theta} = \frac{1}{\alpha} \left\{ \epsilon \frac{\partial \varphi^{(1)}}{\partial \theta} + \epsilon^2 \frac{\partial \varphi^{(2)}}{\partial \theta} + \epsilon^3 \frac{\partial \varphi^{(3)}}{\partial \theta} \right\} \tag{40}$$

where again $\alpha = (\beta_o + \epsilon^2 \beta_2)r$. Performing the Taylor series expansion about $\beta_o r$ and neglecting terms higher than third order in ϵ gives:

$$v(\alpha,\theta,t) = \epsilon \left\{ \frac{\partial \varphi^{(1)}}{\partial \alpha}(\beta_o r) + \epsilon^2 \beta_2 r \frac{\partial^2 \varphi^{(1)}}{\partial \alpha^2}(\beta_o r) \right\} + \epsilon^2 \frac{\partial \varphi^{(2)}}{\partial \alpha}(\beta_o r)$$

$$+ \epsilon^3 \frac{\partial \varphi^{(3)}}{\partial \alpha}(\beta_o r) \tag{41}$$

$$w(\alpha,\theta,t) = \frac{1}{\beta_o r} \left\{ \epsilon \frac{\partial \varphi^{(1)}}{\partial \theta}(\beta_o r) + \epsilon^2 \frac{\partial \varphi^{(2)}}{\partial \theta}(\beta_o r) + \epsilon^3 \left[\frac{\partial \varphi^{(3)}}{\partial \theta}(\beta_o r) \right.\right.$$

$$\left.\left. - \zeta_2 \frac{\partial \varphi^{(1)}}{\partial \theta}(\beta_o r) + \beta_2 r \frac{\partial^2 \varphi^{(1)}}{\partial \alpha \partial \theta}(\beta_o r) \right] \right\} \tag{42}$$

Introducing expressions for the velocity potentials from Eqs. (7), (13), and (20), performing the indicated differentiations, and grouping like harmonics together yields:

$$v(\alpha,\theta,t) = \left\{ \epsilon R_n'(\alpha) + \epsilon^3 \left[F_5'(\alpha) - \zeta_2 R_n'(\alpha) - \zeta_2 \alpha \left(1 - \frac{n^2}{\alpha^2}\right) R_n(\alpha) \right] \right\} \sin(t + n\theta)$$

$$+ \epsilon^2 \left[R_n(\alpha) R_n'(\alpha) - \frac{\gamma + 1}{2} f'(\alpha) \right] \sin 2(t + n\theta)$$

$$+ \epsilon^3 F_1'(\alpha) \sin 3(t + n\theta) \tag{43}$$

$$w(\alpha,\theta,t) = \frac{n}{\alpha}\left\{ \epsilon R_n(\alpha) + \epsilon^3\left[F_5(\alpha) + \zeta_2(\alpha R_n'(\alpha) - R_n(\alpha))\right] \right\} \cos(t+n\theta)$$

$$+ \frac{n}{\alpha}\,\epsilon^2\left[R_n^2(\alpha) - (\gamma+1)f(\alpha) \right] \cos 2(t+n\theta)$$

$$+ \frac{3n}{\alpha}\,\epsilon^3 F_1(\alpha) \cos 3(t+n\theta) \qquad (44)$$

These expressions can be used to determine the magnitude of the steady flow driven by the spinning wave. Since only the radial component contributes to a through flow, only Eq. (43) for v is of concern here. The steady through flow is obtained by taking the time average of v over one period of oscillation. Since the radial velocity consists entirely of terms which are sinusoidal in $(t + n\theta)$ (fundamental with second and third harmonics), the time average of v is zero. There is no steady or time-independent term. Thus the Maslen and Moore analysis predicts no steady flow generated by nonlinearities in the wave motion when the pressure perturbation is required to vanish at the boundaries. This result appears to be independent of the difficulty in satisfying the boundary conditions for the second order solutions.

Typical Numerical Solutions. The expressions derived above for the pressure perturbation P' (Eq. (38)) and the velocity components v and w (Eqs. (43) and (44)) were used to obtain numerical solutions for a typical spinning wave engine configuration. In these calculations an annular pancake geometry was assumed with the ratio of central hole diameter to disk diameter ν of 0.2. The working fluid was assumed to be air with a specific heat ratio γ of 1.4, since combustion is not considered in this analysis.

Finally a first tangential (i.e., $n = 1$, $k = 1$) spinning mode was assumed with an amplitude parameter ϵ of 0.3.

Before the acoustic pressure and velocity can be calculated the following functions are needed: the radial eigenfunction $R_n(\alpha)$ and its derivative, the second order function $f(\alpha)$ and its derivative, and the third order functions $F_1(\alpha)$ and $F_5(\alpha)$ and their derivatives. The radial eigenfunction for the first tangential mode has already been shown in Fig. 3 where $\beta_o = 4.2357$. The second order functions $f(\alpha)$ and $f'(\alpha)$ are shown in Fig. 6 for $\nu = 0.2$ and $\gamma = 1.4$. From these and the radial eigenfunctions, Eqs. (17) and (18) yield the second order pressure functions $P_{20}(\alpha)$ and $P_{23}(\alpha)$ which are plotted in Fig. 7. In order to obtain the third order functions $F_1(\alpha)$ and $F_5(\alpha)$, Eq. (36) was used to yield $\beta_2 = -.49254$. The function $F_1(\alpha)$ and the corresponding pressure function $P_{30}(\alpha)$ (obtained from Eq. (25)) are shown in Figure 8, while Figure 9 shows $F_5(\alpha)$ and the function $P_{34}(\alpha) + \alpha \zeta_2 R_n'(\alpha)$ (obtained from Eq. (26) and (38)).

Pressure waveforms for the spinning first tangential mode were computed using Eq. (38) for two radial stations: $r = 0.56$ where $R_1(\alpha)$ has a maximum (pressure antinode) and $r = 0.8$. These waveforms are plotted in Fig. 10 for both second order (ϵ^3 terms neglected) and third order (ϵ^3 terms retained) approximations with $\epsilon = 0.3$. At $r = 0.56$ the second order waveforms are only slightly distorted from a sinusoidal shape since $P_{20}(\alpha)$ is relatively small, while at $r = 0.8$ the second harmonic distortion is readily apparent for here $P_{20}(\alpha)$ attains nearly its maximum magnitude. Adding

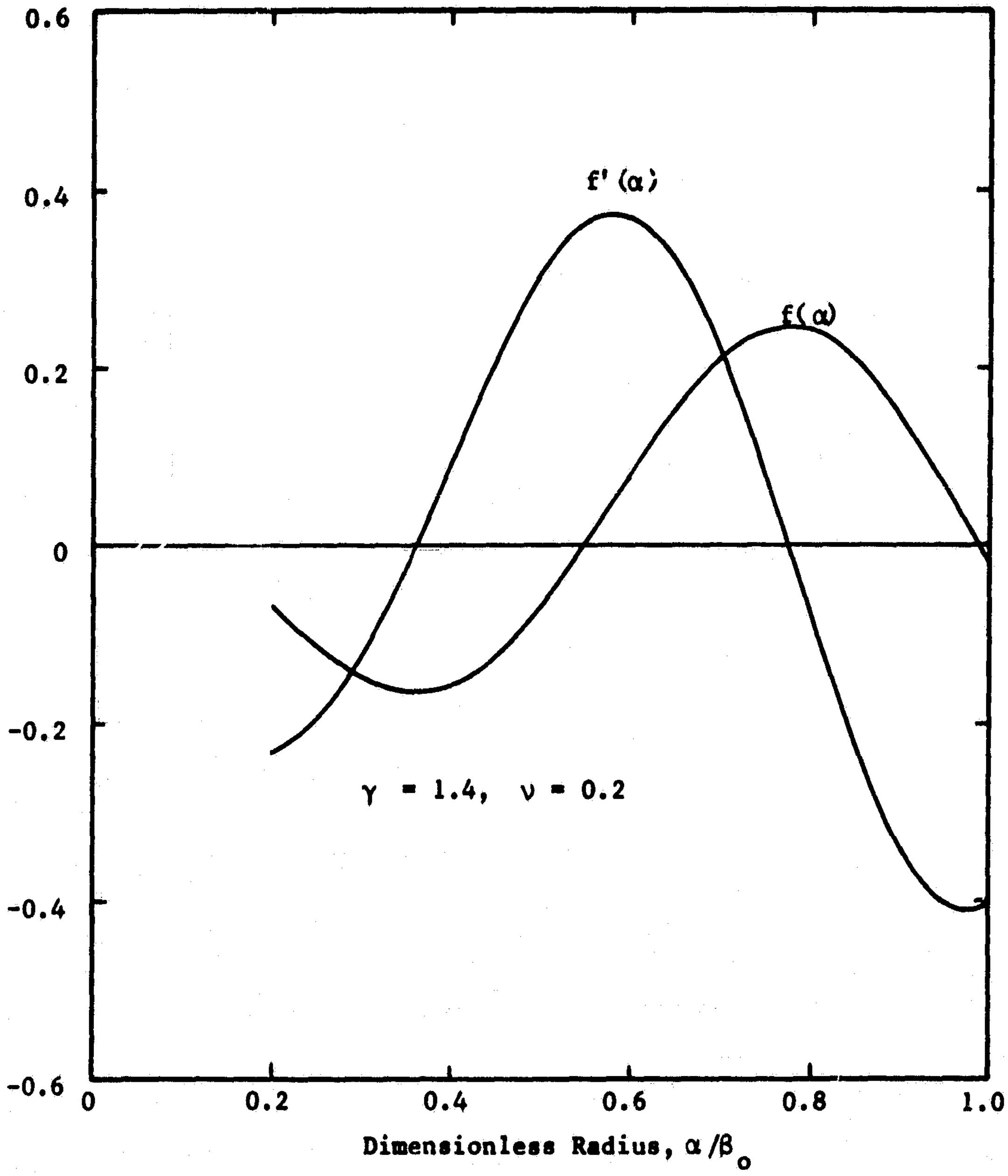

Figure 6. Second Order Function f(α) and Its Derivative for the Spinning 1T Mode.

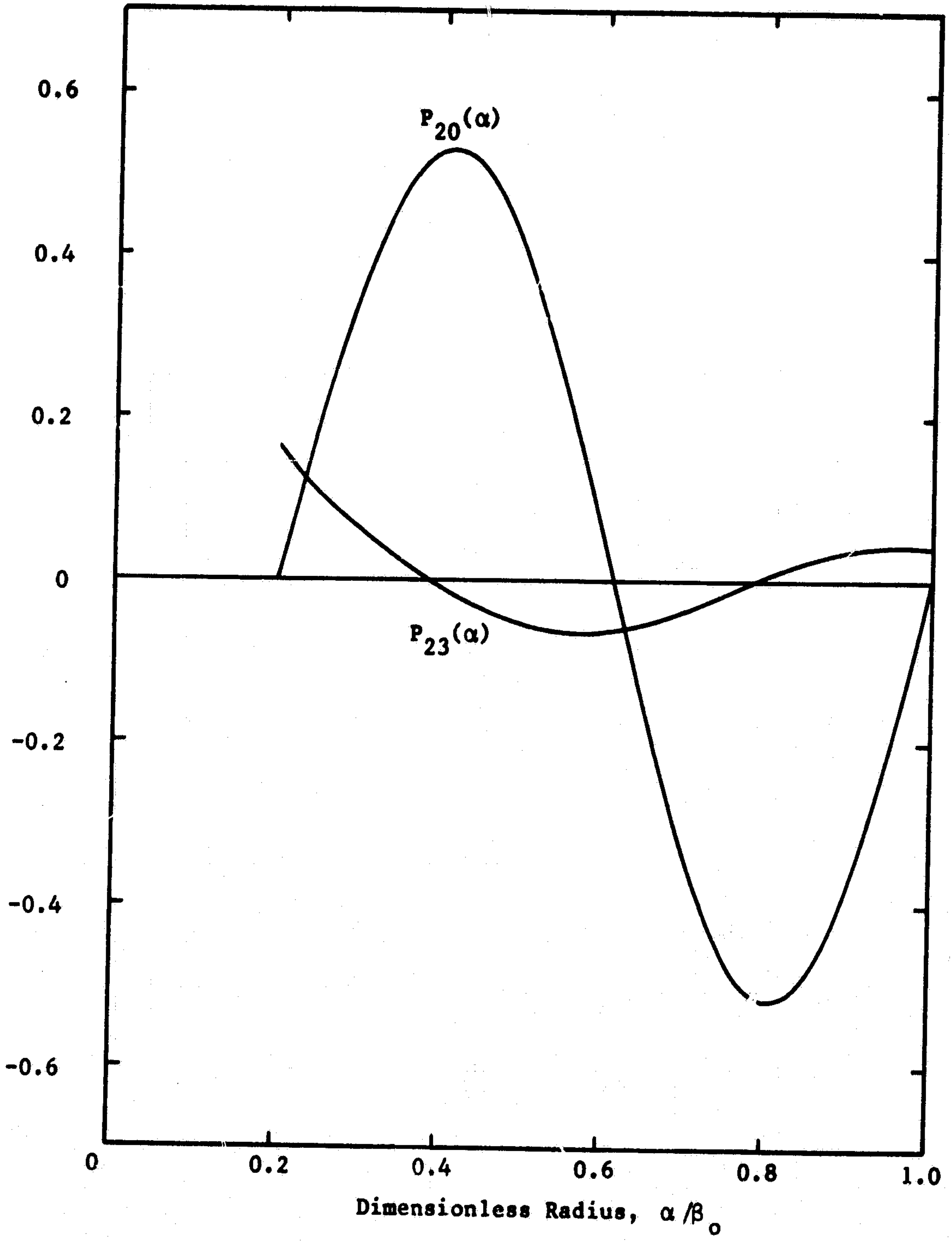

Figure 7. Second Order Pressure Functions for the Spinning 1T Mode.

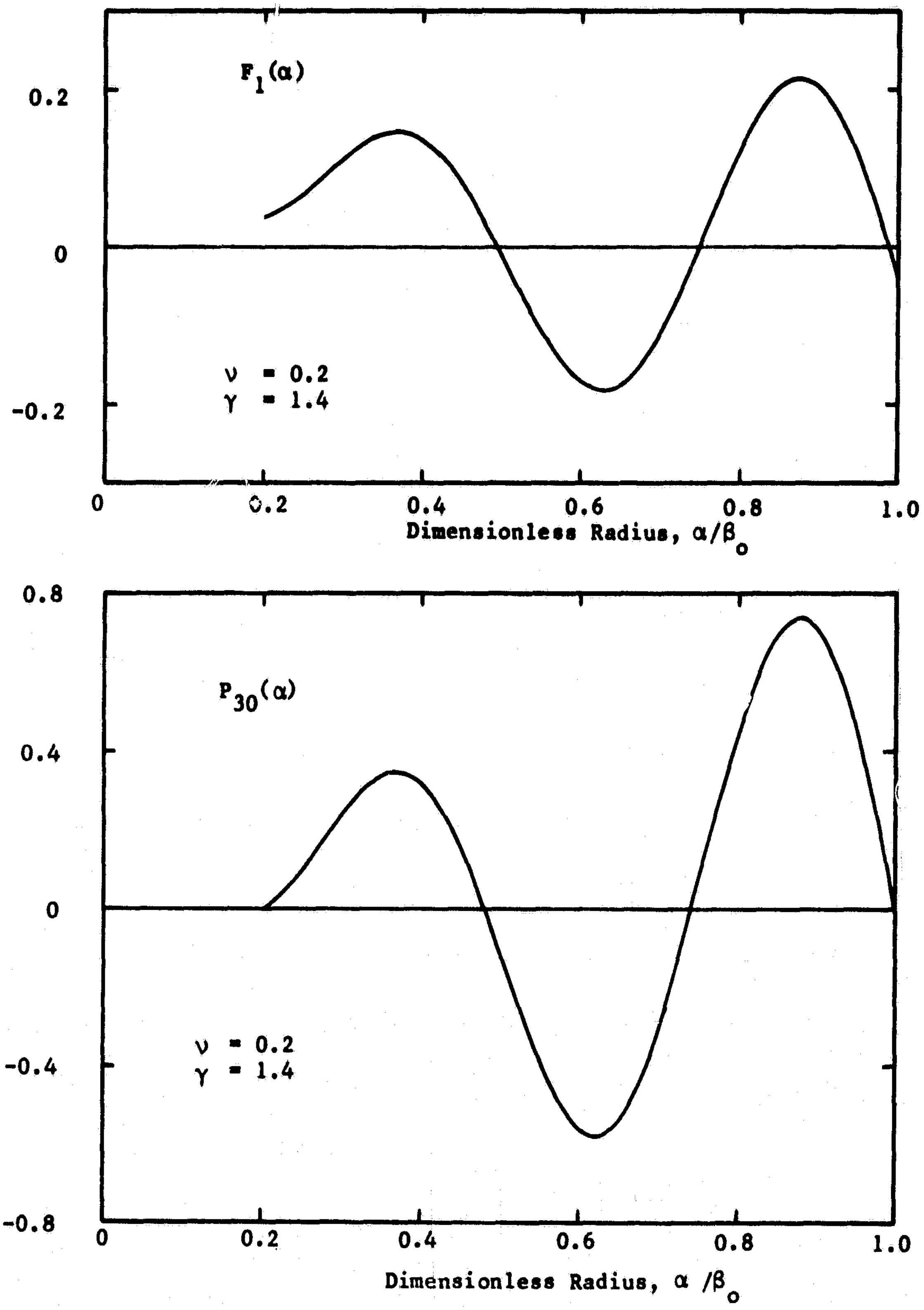

Figure 8. Third Order Function $F_1(\alpha)$ and Corresponding Pressure Function $P_{30}(\alpha)$ for Spinning 1T Mode.

ORIGINAL PAGE IS
OF POOR QUALITY

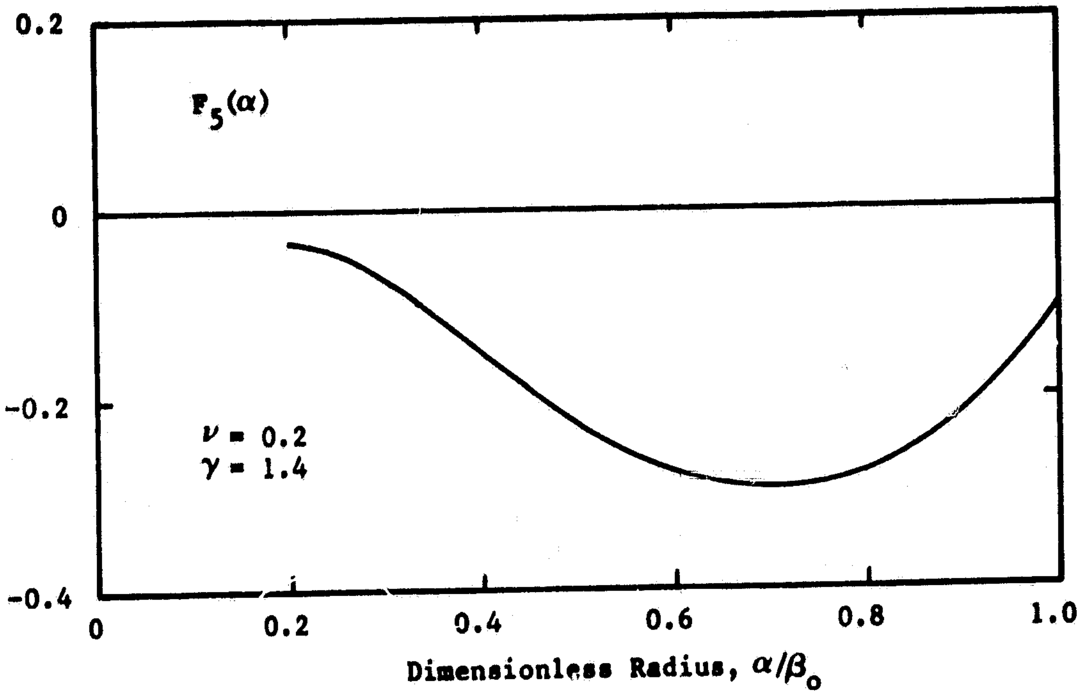

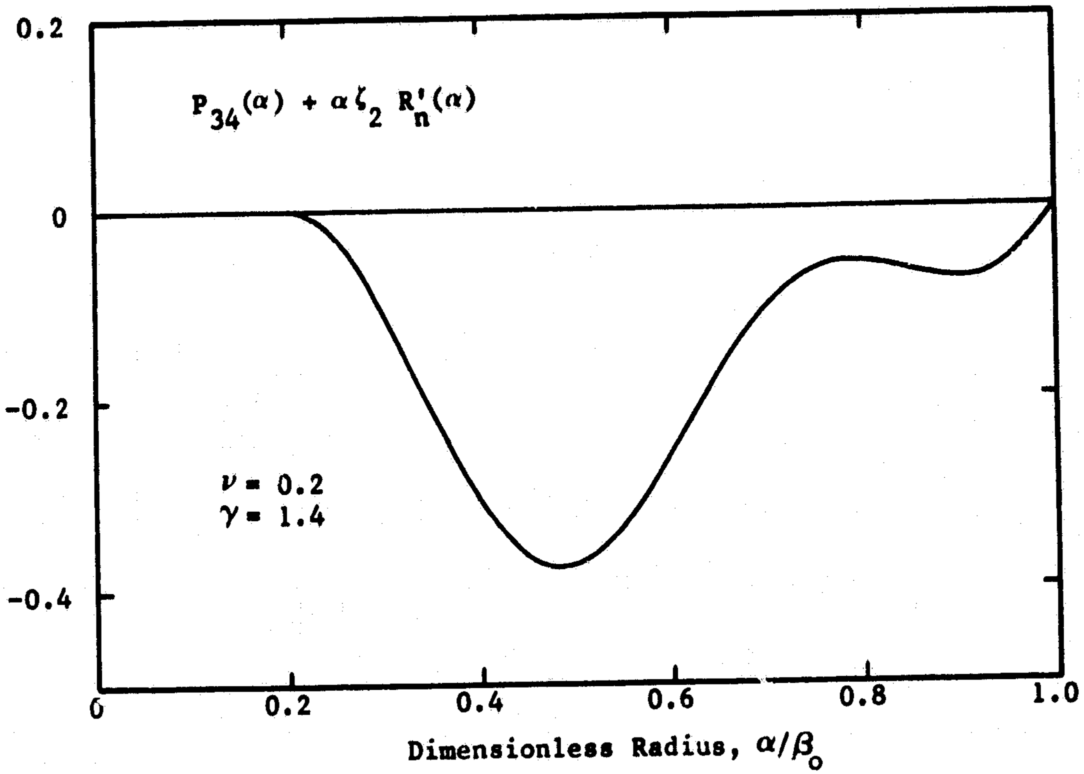

Figure 9. Third Order Function $F_5(\alpha)$ and Corresponding Pressure Function $P_{34}(\alpha)$ for Spinning 1T Mode.

the third order terms tends to flatten the peaks at $r = 0.56$ and smooth out the minima at $r = 0.8$. At the boundaries $r = 0.2$ and $r = 1.0$ the oscillatory component of the pressure vanishes, however a time independent component or mean pressure shift remains. This boundary residual which was discussed previously (Eqs. (32)) amounts to about - 2% of the ambient pressure at the inner boundary and about - 0.5% of the ambient pressure at the outer boundary for $\epsilon = 0.3$.

The radial velocity waveforms were calculated using Eq. (43) at the boundaries where they attain their maximum amplitude. These waveforms are shown in Figure 11 for both second order and third order approximations. The principal effect of nonlinearities on the velocity waveforms is to steepen the rising portion of the curve and flatten the descending branch while preserving symmetry about zero velocity. This is more apparent at the outer boundary $r = 1$. Due to this symmetry, there is no steady flow through the system.

The effect of amplitude upon frequency is determined from Eq. (27) as:

$$\frac{\omega}{\omega_o} = \frac{f}{f_o} = \frac{\beta}{\beta_o} = 1 + \epsilon^2 \frac{\beta_2}{\beta_o} \quad \text{or}$$

$$\frac{f}{f_o} = 1 + \zeta_2 \epsilon^2 \tag{45}$$

For the present case, $\beta_2 = -.49254$ for which $\zeta_2 = -.11628$. Thus frequency is seen to decrease as the amplitude parameter is increased. A similar variation of frequency with amplitude was calculated by Maslen and

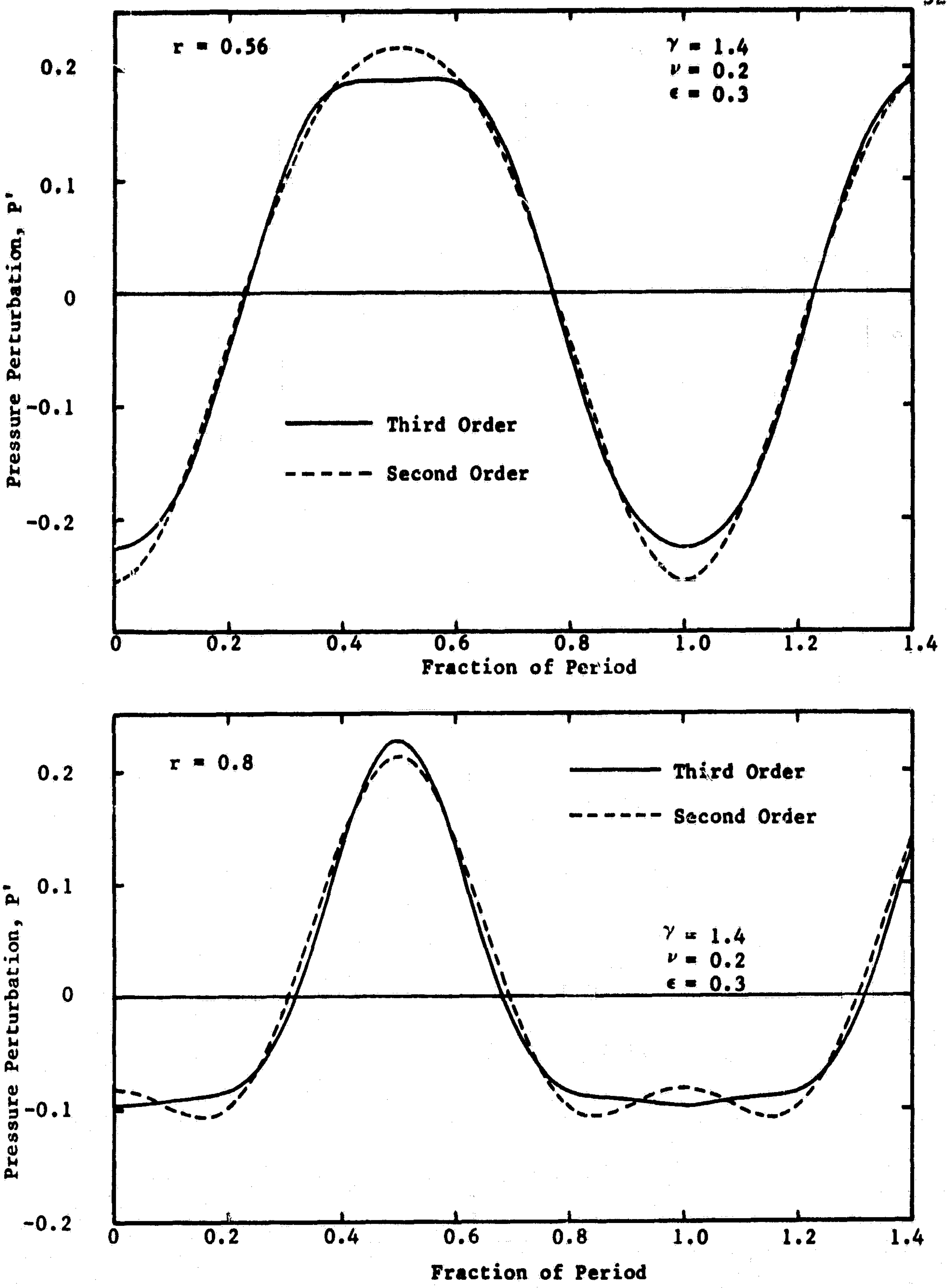

Figure 10. Pressure Waveforms for Spinning 1T Mode.

ORIGINAL PAGE IS
OF POOR QUALITY

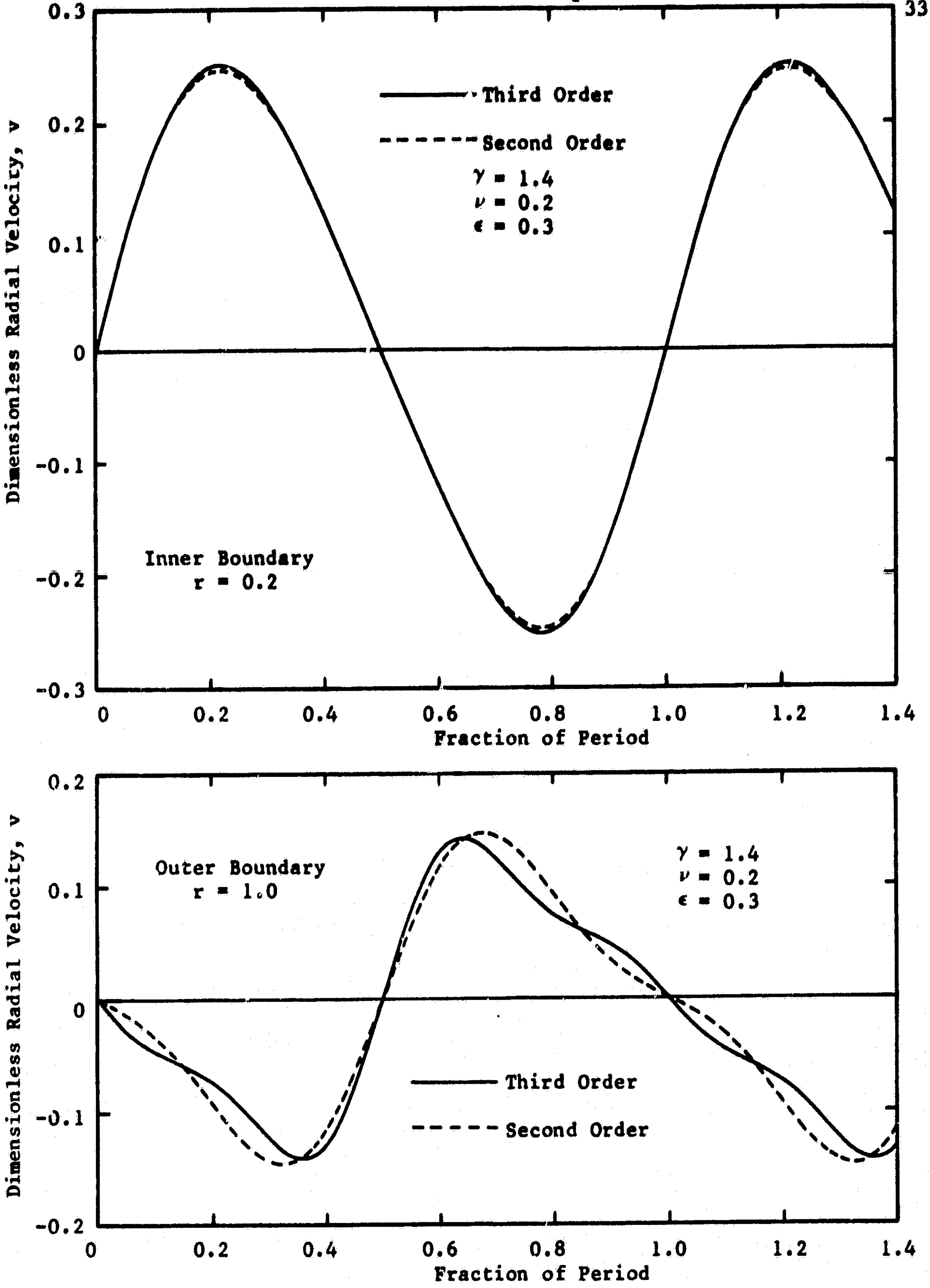

Figure 11. Boundary Radial Velocity Waveforms for the Spinning 1T Mode.

Moore for the hard-walled cylinder with $\zeta_2 = -0.084$. For $\epsilon = 0.3$ the frequency shift is quite small, giving a frequency only about one percent less than the acoustic frequency.

Analysis with Steady Potentials

The straightforward application of the perturbation technique of Maslen and Moore to the open annular cavity does not yield an acoustically driven steady through flow as shown by Eq. (43). In this analysis the solutions assumed for $\varphi^{(1)}$, $\varphi^{(2)}$, and $\varphi^{(3)}$ were patterned after the solutions assumed by Maslen and Moore which did not explicitly contain a steady flow term. In this problem, however, a steady flow term is permissible since the boundaries are open. In an attempt to predict acoustic pumping, the Maslen and Moore approach will be modified by including a steady potential in the solutions for $\varphi^{(1)}$, $\varphi^{(2)}$ and $\varphi^{(3)}$.

The analysis is modified by adding a steady potential to each of the unsteady potentials used previously. Thus the velocity potential becomes

$$\varphi = \epsilon\left[\varphi^{(1)} + \bar{\varphi}^{(1)}\right] + \epsilon^2\left[\varphi^{(2)} + \bar{\varphi}^{(2)}\right] + \epsilon^3\left[\varphi^{(3)} + \bar{\varphi}^{(3)}\right] + \dots \tag{46}$$

where the steady potentials $\bar{\varphi}^{(i)}$ are functions of α and θ and the sum of the potentials $\varphi^{(i)} + \bar{\varphi}^{(i)}$ must satisfy Eqs. (5), (12), and (19). The existence of $\bar{\varphi}^{(1)}$, however, implies the existence of acoustic pumping in the first order or linear regime (small amplitude). Since acoustic pumping is expected to arise from the nonlinearities of the system, it will be postulated that the first order steady potential is zero. Thus the first order solution for the velocity potential is still given by Eq. (7) and the first order pressure is still given by Eq. (10).

The second order solutions are determined by replacing $\varphi^{(2)}$ in the left-hand-side of Eq. (12) with $\varphi^{(2)} + \bar{\varphi}^{(2)}$ and using Eq. (7) in the right-hand-side for $\varphi^{(1)}$. This yields $\varphi^{(2)}$ as given by Eqs. (13) and (14) while $\bar{\varphi}^{(2)}$ must satisfy Laplace's Equation:

$$\nabla^2 \bar{\varphi}^{(2)} = 0 \qquad (47)$$

Due to symmetry considerations the steady flow driven by a spinning acoustic mode is expected to be independent of the angular coordinate θ. Solutions of Laplace's Equation which satisfy this criterion are the potential source or sink which is a purely radial flow and the potential vortex which is a purely tangential flow. Although only the radial flow component can contribute to a mean flow through the annular cavity, there is no apparent physical reason to exclude the vortex flow component. Since the acoustic wave rotates around the chamber, it is quite likely that a vortex flow is generated. Since Laplace's Equation is linear, superposition of solutions is permitted, and the steady potential $\bar{\varphi}^{(2)}$ will be assumed to be a linear combination of source and vortex flows given by:

$$\bar{\varphi}^{(2)} = K_s \ln\alpha + K_v \theta \qquad (48)$$

where K_s and K_v are constants to be determined.

The second order contribution to the pressure $P^{(2)}$ is obtained by substituting $\varphi^{(1)}$ and $\varphi^{(2)} + \bar{\varphi}^{(2)}$ into the right-hand-side of Eq. (15). Since $\varphi^{(1)}$ contains no steady component and $\bar{\varphi}^{(2)}_t = 0$ (by definition) the expression for $P^{(2)}$ is unaffected by the second order steady potential $\bar{\varphi}^{(2)}$.

Thus $p^{(2)}$ is still given by Eqs. (16), (17) and (18). From this result it is seen that including the second order steady potentials does not remedy the difficulty in satisfying the pressure boundary conditions to second order.

The third order solutions are obtained by introducing Eq. (7) for $\varphi^{(1)}$ and $\varphi^{(2)} + \bar{\varphi}^{(2)}$ given by Eqs. (13) and (48) into the right-hand-side of Eq. (19). Expanding the right-hand-side, collecting terms, and using $\varphi^{(3)} + \bar{\varphi}^{(3)}$ in the left-hand-side yields the solution for $\varphi^{(3)}$ as:

$$\varphi^{(3)} = F_1(\alpha)\sin 3(t+n\theta) + F_4(\alpha)\cos(t+n\theta) + F_5(\alpha)\sin(t+n\theta) \tag{49}$$

where $F_1(\alpha)$ satisfies Eq. (21) as before, but, $F_4(\alpha)$ and $F_5(\alpha)$ are solutions of the following inhomogeneous equations:

$$F_4'' + \frac{1}{\alpha} F_4' + \left(1 - \frac{n^2}{\alpha^2}\right) F_4 = \frac{2K_s}{\alpha} R_n'(\alpha) \tag{50}$$

$$F_5'' + \frac{1}{\alpha} F_5' + \left(1 - \frac{n^2}{\alpha^2}\right) F_5 = \mathcal{R}_5(\alpha) - \frac{2nK_v}{\alpha^2} R_n(\alpha) \tag{51}$$

where $\mathcal{R}_5(\alpha)$ is given by Eq. (B-16) as before. The steady potential $\bar{\varphi}^{(3)}$ must also satisfy Laplace's Equation:

$$\nabla^2 \bar{\varphi}^{(3)} = 0 \tag{52}$$

The third order contribution to the pressure is obtained from Eq. (23) using Eqs. (7), (13), (48) and (49) to yield:

$$p^{(3)} = -\gamma \left\{ P_{30}(\alpha)\cos 3(t+n\theta) + P_{33}(\alpha)\sin(t+n\theta) + P_{34}(\alpha)\cos(t+n\theta) \right\} \tag{53}$$

where $P_{30}(\alpha)$ is given by Eq. (25) as before, while $P_{33}(\alpha)$ and $P_{34}(\alpha)$ are given by:

$$P_{33}(\alpha) = -F_4(\alpha) + \frac{K_s}{\alpha} R_n'(\alpha) \tag{54}$$

$$P_{34}(\alpha) = G_5(\alpha) + \frac{nK_v}{\alpha^2} R_n(\alpha) \tag{55}$$

where $G_5(\alpha)$ is the right-hand-side of Eq. (26).

It is seen from the above analysis that including a steady term in the second order potential $\bar{\varphi}^{(2)}$ affects only the third order contribution to the pressure through the new term $P_{33}(\alpha)\sin(t+n\theta)$ and by modifying $P_{34}(\alpha)$. This effect can be viewed as shifting the phase and changing the amplitude of the third order pressure component which oscillates at the fundamental frequency. A similar effect occurs in the third order potential through the new function $F_4(\alpha)$ and a modification of $F_5(\alpha)$.

The boundary conditions are applied using the Taylor series expansions as before with the eigenvalue β expanded according to Eq. (28). Again the first order correction β_1 vanishes and the boundary conditions on $f(\alpha)$ are again specified by Eqs. (31). The third order function $F_1(\alpha)$ also satisfies the same boundary conditions as derived previously; namely, those given by Eqs. (34). The boundary conditions on $F_5(\alpha)$ are also the same as before, since the contribution of the vortex flow to $P_{34}(\alpha)$ vanishes at the boundaries (see Eq. (56)). Thus the boundary conditions for $F_5(\alpha)$ are given by Eqs. (35) in terms of β_2. However the solution for $F_5(\alpha)$ depends upon the vortex flow K_v through the additional term on the right of Eq. (51). The pressure boundary conditions also require that $P_{33}(\nu\beta_o) = P_{33}(\beta_o) = 0$

which from Eq. (54) yields:

$$F_4(\beta_o) = \frac{K_s}{\beta_o} R_n'(\beta_o) \tag{57a}$$

$$F_4(\nu\beta_o) = \frac{K_s}{\nu\beta_o} R_n'(\nu\beta_o) \tag{57b}$$

Solutions for $F_4(\alpha)$ and $F_5(\alpha)$ are given in Appendix C. It is also shown in Appendix C that the boundary conditions do not provide enough information to uniquely determine the frequency correction β_2, the steady flow parameters K_s and K_v, and the constants of integration appearing in the functions $F_4(\alpha)$ and $F_5(\alpha)$. Furthermore, it is shown that there is no value of K_s for which Eqs. (57) are satisfied.

From the above analysis, it appears that adding steady flow terms to the Maslen and Moore analysis does not provide a means for predicting whether a large amplitude spinning wave can generate a steady flow through an open annular cavity.

TEST MODEL AND INSTRUMENTATION

Test Model

An illustration of the spinning wave engine test model is in Figure 12. The assembled model is shown in the photographs of Figure 13. Two parallel, 61 cm (24") diameter discs are used to form the cylindrical cavity for the spinning wave. The cavity is open to the environment around the entire periphery and at central ports 12.2 cm (4.8") in diameter ($\nu = 0.2$). The spacing between the discs is variable via the four threaded support rods located outside the cavity. One disc is fabricated from 2.5 cm thick, transparent plexiglas to allow flow visualization. The other disc is fabricated from 1.25 cm thick aluminum plate. Four acoustic drivers, at 90° intervals, are mounted to the aluminum disc with the active surface flush with the internal surface. The model is equipped with ten ports for flush mounting 2.5 cm microphones. Three of these, which are clearly visible in the photographs, are along a radial line on the plexiglas disc. Seven are on the aluminum disc along a radial line and at three circumferential positions at 90° intervals. The radial location of these circumferential microphone ports and the acoustic drivers coincides with the pressure antinode predicted by the acoustic solution. Also shown in the photographs, but excluded from the illustration of Figure 12 for the sake of clarity, are five static pressure taps along a radial line on the plexiglas disc.

Figure 14 presents a plan view of the apparatus and shows locations of the various instrumentation and the corresponding nomenclature used herein. The four drivers are indicated as $D1_A$, $D1_B$, $D2_A$, and $D2_B$. The

ORIGINAL PAGE IS
OF POOR QUALITY

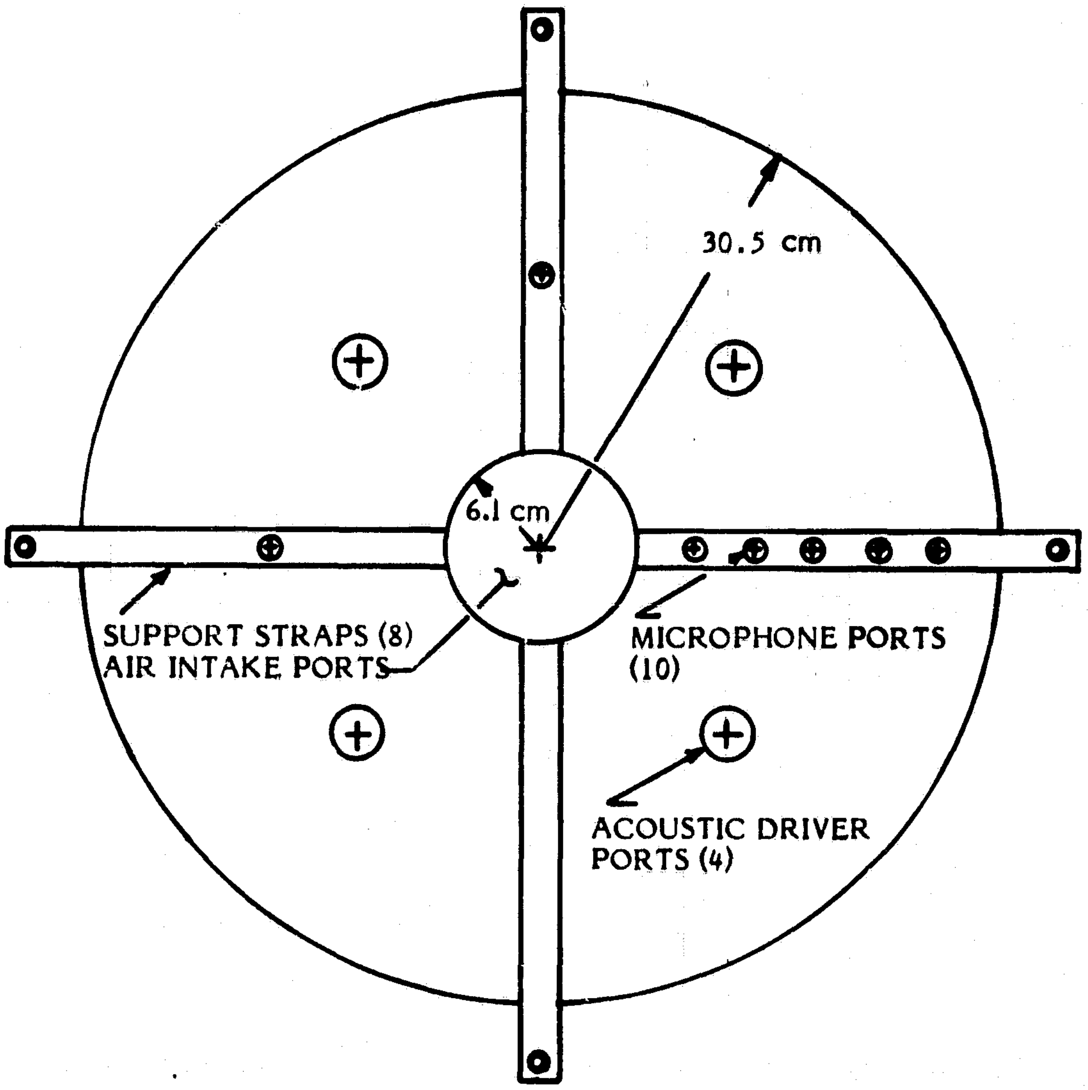

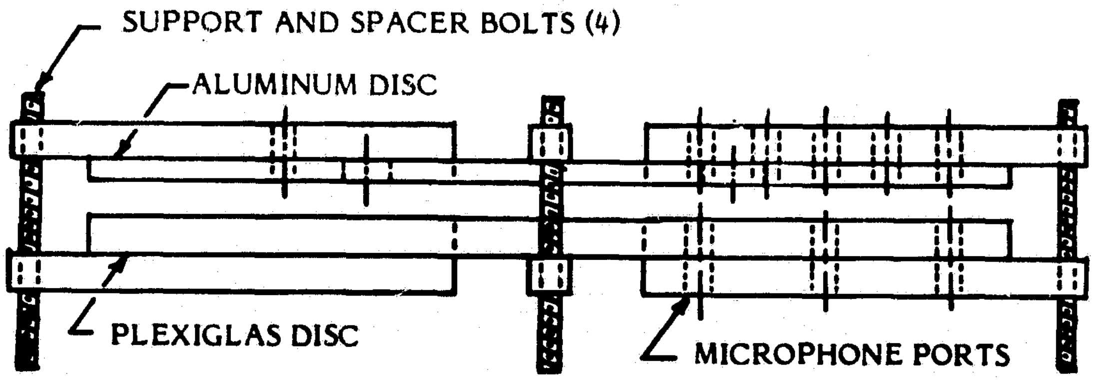

Figure 12. Spinning Wave Engine Test Model.

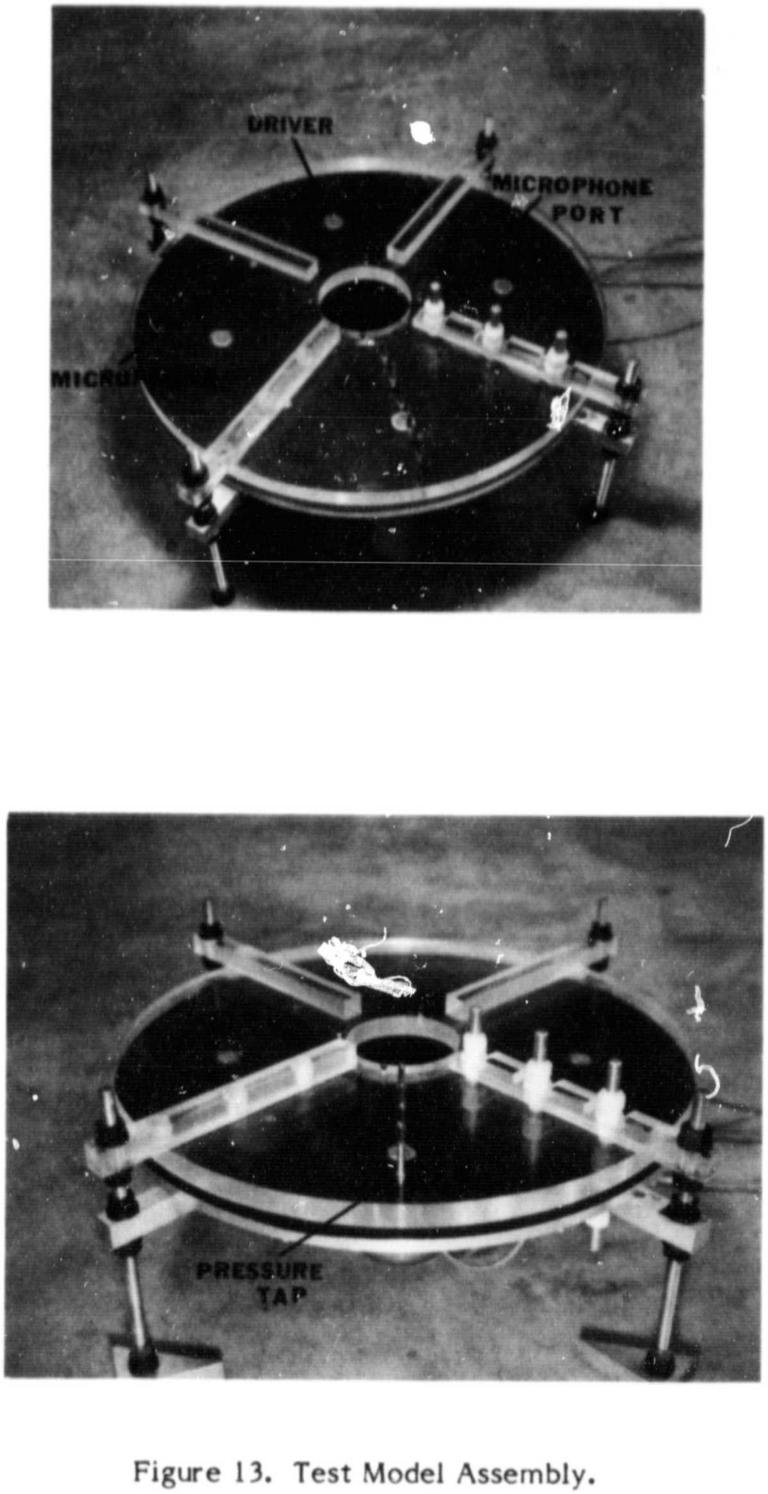

Figure 13. Test Model Assembly.

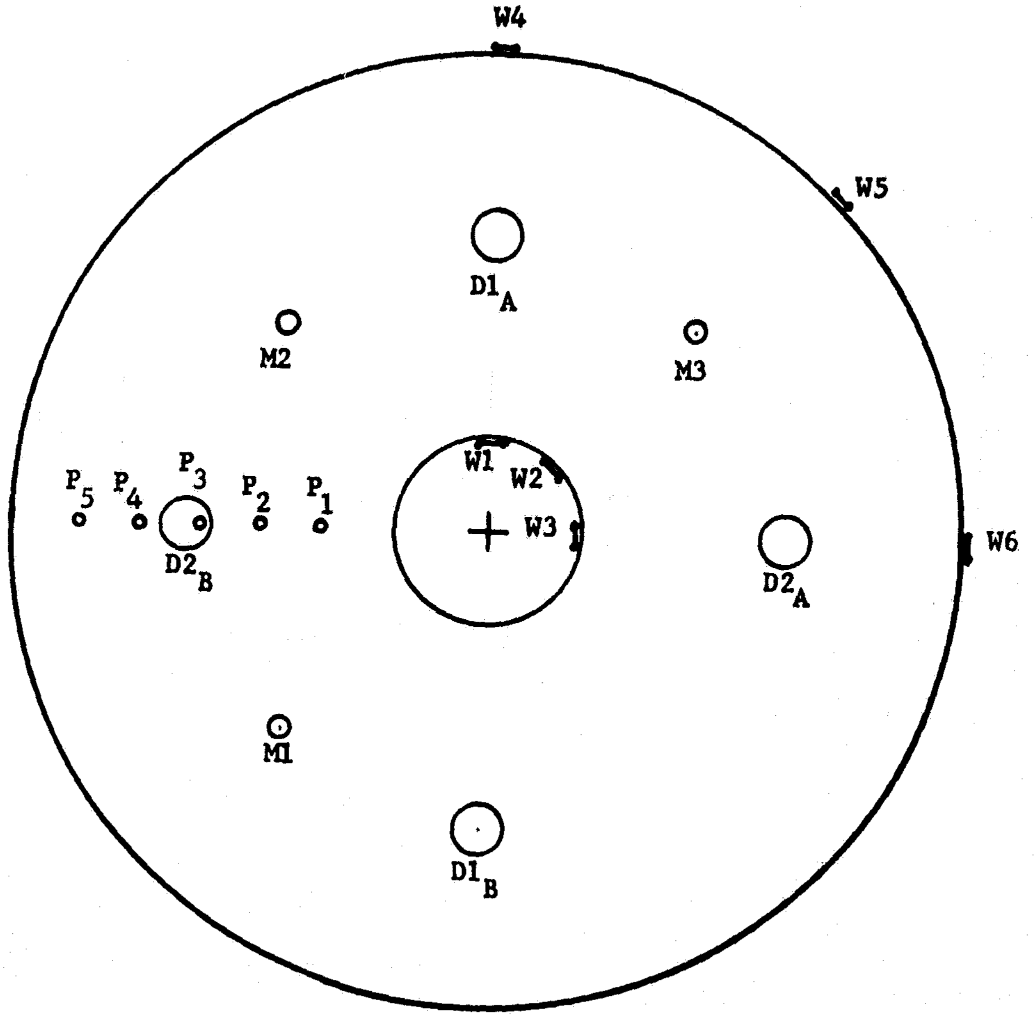

Figure 14. Schematic of Driver, Microphone, and Hot-Wire Locations.

microphones, M1, M2, and M3, are shown at the primary locations for the spinning wave tests. The static pressure ports indicated by P_1 through P_5 are equally spaced along a radial line. P_3 is located on the surface opposite to that of $D2_B$. Finally, six locations used for the constant temperature hot wire measurements are shown as W1 through W6. These cover one quadrant of the flow field with spacings at 45° intervals at both the inner and outer radius of the cavity.

Instrumentation

Four 75 watt University drivers, Model ID-75, were used to excite the oscillatory flows. In most cases, the four drivers were operated in pairs with $D1_A$ and $D1_B$ as one pair and $D2_A$ and $D2_B$ as the other. Each pair was powered by a single Krohn-Hite 50 watt amplifier, Model DCA-50R, and 50 watt matching transformer, Model MT-56. The two drivers of a pair were excited 180° out of phase by reversing the polarity of input leads. A Hewlett Packard Model 203A two-channel, variable phase function generator was used to provide simple harmonic input signals to the two amplifiers. Operation with any combination of from one to four drivers was possible by connecting or unconnecting input leads.

Three B & K condenser microphone cartridge type 4134 were used for measuring the oscillatory pressures. The microphones could be relocated to any of the ten microphone ports shown in Figures 12 and 13 by interchanging microphones and cylindrical plugs. Microphone outputs were measured by a B & K type 2606 amplifier with frequency range from 2 to 200,000 Hz.

Hot-wire measurements were made with a TSI single channel hot-wire anemometer system consisting of a constant temperature anemometer module, a monitor and power supply module, and a signal linearizer with a 4th degree polynomial curve fit. A tungsten platinum coated hot wire with a sensor diameter of 5μ, sensor length of 1.25 mm, and upper frequency response of better than 200 kHz was used. Hot-wire outputs were measured both with an averaging voltmeter and a true RMS voltmeter.

Input and output AC signal wave forms were observed and photographed using a Tektronix type 549 oscilloscope equipped with a Polaroid camera attachment. Furthermore, phases between the various AC signals were measured with a Wavetek phase meter Model 740.

Mean or DC static pressures were measured using a highly stable and accurate Datametrics Barocel Electronic Manometer with a 10 mm Hg variable capacity pressure transducer. Measurements are accurate to 1% of reading over the range from about 95 to 175 dB.

Calibrations

The microphones were calibrated with the standard B & K Pistonphone type 4220. The hot-wire calibration of voltage output versus flow velocity was provided by TSI. This calibration, which was made using their low velocity, steady flow calibrator, covered the range of from 0 to 6 m/s. The calibration data was fitted to a fourth degree polynomial of velocity versus voltage within a velocity accuracy of better than 1% for all test conditions reported herein. The analog circuitry of the anemometer linearizer were set using the coefficients of the polynomial so that the output voltage was equal to the velocity. Thus, assuming quasi-steady flow over the wire, as is the practice for turbulent flow measurements, the linearizer output yields a faithful representation of the velocities and velocity wave forms.

Since the drivers are mechanical devices with inertia the output and input signals cannot be perfectly in phase. Of more importance, differences in the mechanical drivers will cause differences between the phases of the output and input signals. Checks of the drivers used in this investigation indicated that the output signals from the various drivers could be out of phase by as much as 5° for the same input signal. This is relatively small in comparison with the 90° and 180° phase shifts used for the tests reported herein. Nevertheless, it does mean that it was not possible to obtain a perfect spinning wave, but, instead, the superpositioning of a predominant spinning wave on a weak standing wave was obtained. However, the existence of a superimposed weak standing wave does not alter the meaning or conclusions from the tests.

EXPERIMENTAL RESULTS AND DISCUSSION

The experimental investigations include measurements of the resonant frequencies within the cylindrical cavity, phase changes for transition from standing to spinning wave modes, radial distributions of the oscillatory (AC) and mean (DC) pressures, and simultaneous hot-wire and microphone data. In addition, flow visualization studies were made as a qualitative verification of the hot-wire results. The results are presented and discussed in the following sections. It is important to point out that exploratory studies yielding meaningful qualitative rather than more exact quantitative results were emphasized in order to maximize the benefits for the time available.

Resonant Frequencies and Transition from Standing to Spinning Waves

Natural frequencies of oscillations in the cylindrical cavity are indicated by the results of Figure 15 which presents plots of the RMS pressures measured by two microphones as a function of driver frequency. Results are shown for two power levels. For each power level, the driver input power was maintained while the excitation frequency was varied. Resonance occurs where the RMS pressures peak.

Figure 15a shows results for the standing-wave mode of operation excited by the single driver $D1_A$ (see Figure 14 for driver and microphone nomenclature and locations). The first harmonic occurs at a frequency of 692 Hz. The second and third harmonics are at frequencies of 1065 Hz and 1275 Hz, respectively.

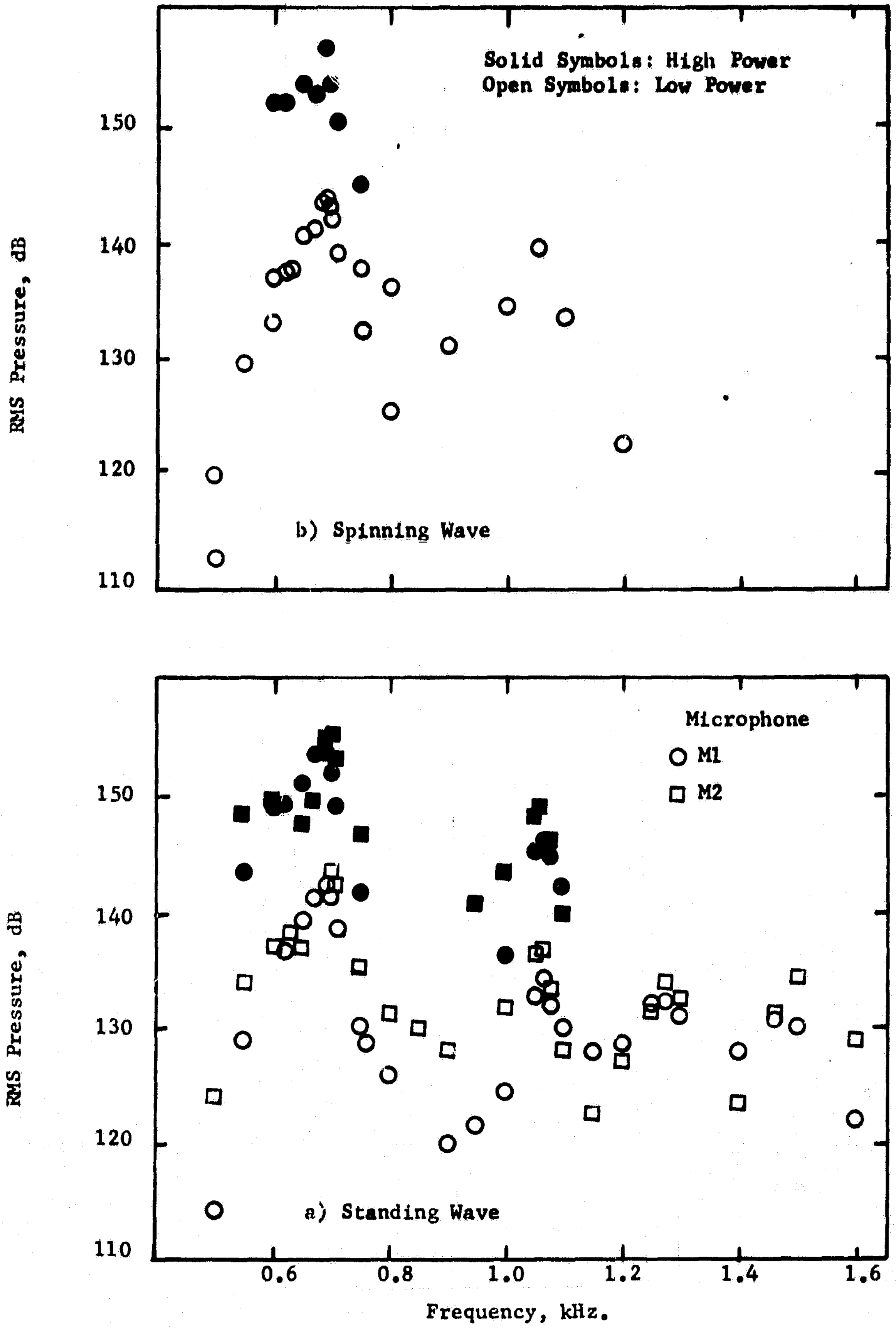

Figure 15. Effect of Driver Frequency upon Oscillatory Pressure. Ambient Temperature = 24°C. Cavity

Figure 15b shows results for the spinning wave mode of operation. Data are included for the spinning wave excited both by the two drivers $D1_A$ and $D2_A$ and by all four drivers ($D1_A$, $D1_B$, $D2_A$, and $D2_B$). In both cases, $D2_A$ is set to lag $D1_A$ by 90°. Also, when using the four drivers, $D1_B$ lags $D1_A$ by 180° and $D2_B$ lags $D2_A$ by 180° since, as discussed before, the input leads for these pairs of drivers are reversed. The resonant frequencies are the same as those of Figure 15a for the standing waves. This is to be expected since these spinning waves represent the superpositioning of the two standing waves oscillating 90° out of phase.

Additional results verifying the natural frequencies are presented in Figure 16. This figure shows power spectra computed from the outputs of microphones M1 and M2 when white noise is used to excite driver $D2_A$. These results were obtained by feeding the real time microphone outputs directly to a Hewlett Packard Fourier analyzer and are based on an ensemble of 100 data strips and a frequency band width of 20 Hz. Because of a slight error in the plotting scale factor the frequencies are shifted slightly toward the higher values (e.g., the cutoff frequency should be precisely 2500 Hz rather than the indicated value of about 2575 Hz). Accounting for this slight shift, the resonance frequencies for the first three harmonics, as indicated by the peaks in the power spectra, are about 700, 1070, and 1275 Hz, in excellent agreement with the results of Figure 15. Also plotted on Figure 16 are computed curves of the magnitude and phase of the transfer function which relates the outputs of M1 and M2. These results show that the two microphones respond in phase and with nearly a one-to-one

ORIGINAL PAGE IS
OF POOR QUALITY

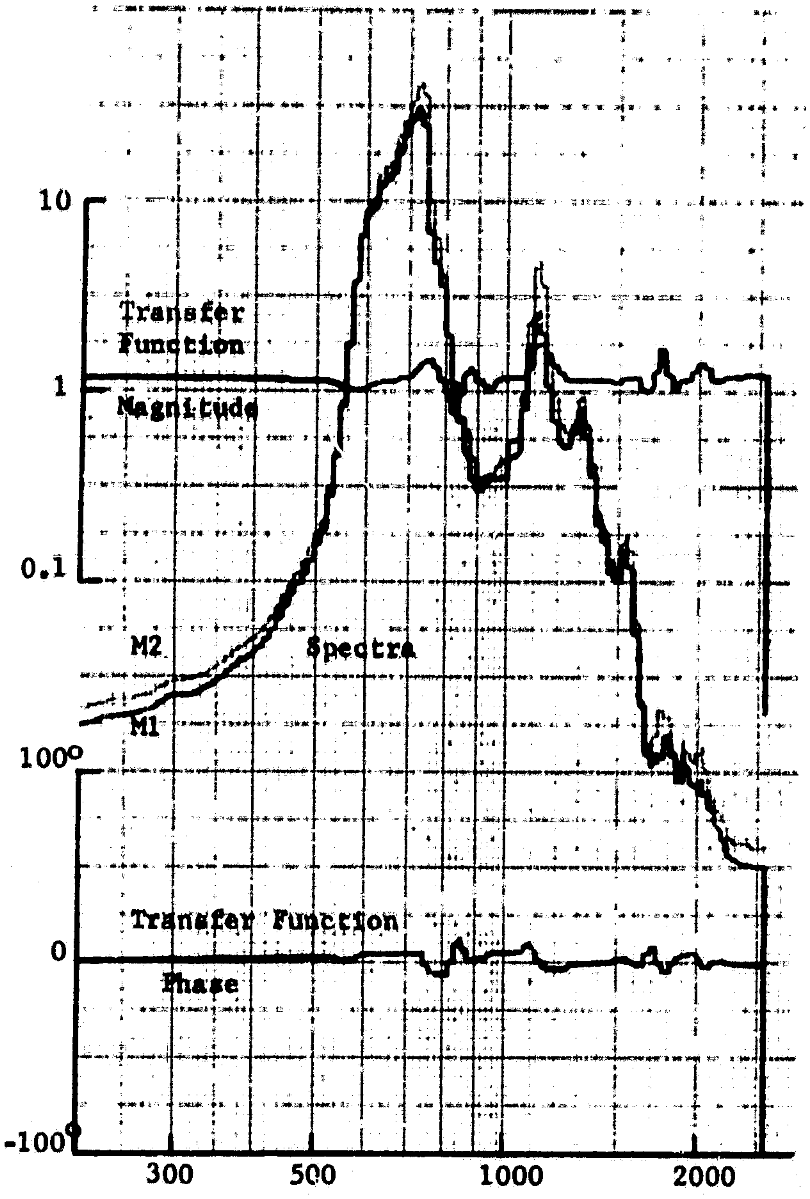

Figure 16. Spectra and Transfer Function for White Noise.

relationship (the magnitude of the transfer function is slightly greater than 1.0 due to differences in the microphones). This and the similarities in the power spectra attest to the quality and symmetries of the model and instrumentation.

The experimental value of 692 Hz for the fundamental frequency is significantly different from the theoretical acoustic value of 760 Hz for ν = 0.2. This cannot be attributed to higher order effects. At the highest pressure level for resonance (RMS pressure = 157 dB) the value of the amplitude parameter ε, as used in the perturbation analysis, is only 0.025. At the lowest pressure level for resonance at the fundamental frequency the value of the amplitude parameter is less than 0.01. Thus, second and higher order terms must be small. It is noted, however, that the experimental frequency is nearly the same as the theoretical acoustic value for a model of the same outer diameter but without a central hole (i.e., $\nu = 0$). This might indicate that the constant-pressure boundary condition is not satisfied at the inner boundary.

Figure 17 is included to illustrate phase changes within the cavity for transition from standing to spinning wave modes of operation. These results were obtained using drivers $D1_A$ and $D2_A$, only, and with $D2_A$ lagging $D1_A$ by 90°. Similar results were obtained using all four drivers but the results were not completely documented. The phase lag between the output of M1 and M2 is plotted against the ratio of the input power to $D2_A$ to that of $D1_A$. The power input to $D1_A$ was held constant while the power input to $D2_A$ was varied. With a power ratio of zero a standing wave exists and the theoretical

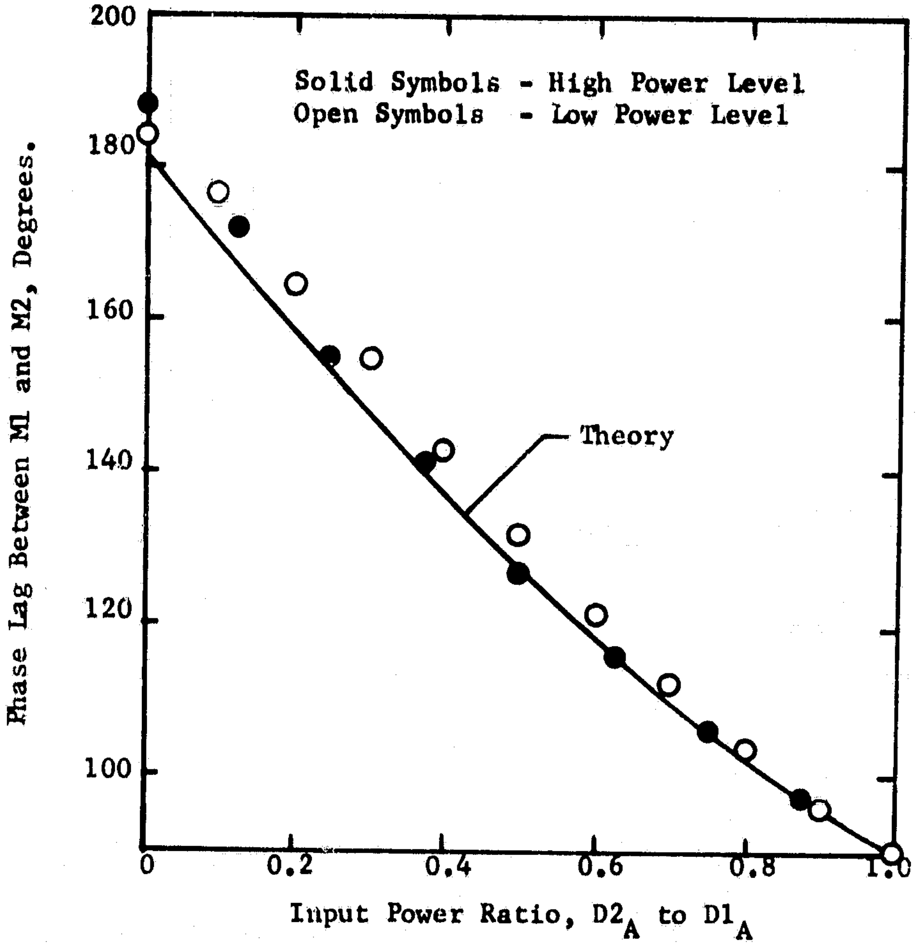

Figure 17. Transition from Standing to Spinning Wave Modes.
f = 692 Hz.

phase lag is 180°. As the power ratio increases two standing waves 90° apart and 90° out of phase are superimposed to produce combined spinning and standing waves. For a power ratio of unity a pure spinning wave is obtained and the theoretical phase between the two microphones, is 90°, corresponding to the angular displacement of 90°. Also shown on Figure 17 is the theoretical curve for the phase lag derived by superimposing standing waves. It can be shown that this theoretical phase lag is the arc-cotangent of the power ratio. The agreement between the theoretical and experimental results shown on Figure 17 is good.

Radial Distributions of Pressures

Figure 18 presents radial distributions of the RMS value of the periodic component of pressure for the spinning wave mode of operation. The pressures are normalized by the value at $r = 1.0$ in order to facilitate a comparison with the theoretical solution. Included in Figure 18 is the acoustic solution which is appropriate for these experimental data since the maximum value of the amplitude parameter ϵ is less than 0.01. As shown by Figure 18, the experimental pressures are in good agreement with the acoustic solution for $0.33 \leq r \leq 0.87$ and it seems that the periodic pressure will decay to zero at the open boundaries where $r = 0.2$ and 1.0. However, the constant pressure boundary condition is not adequately confirmed, and, in retrospect, the test model should have been equipped with microphone ports nearer these open boundaries.

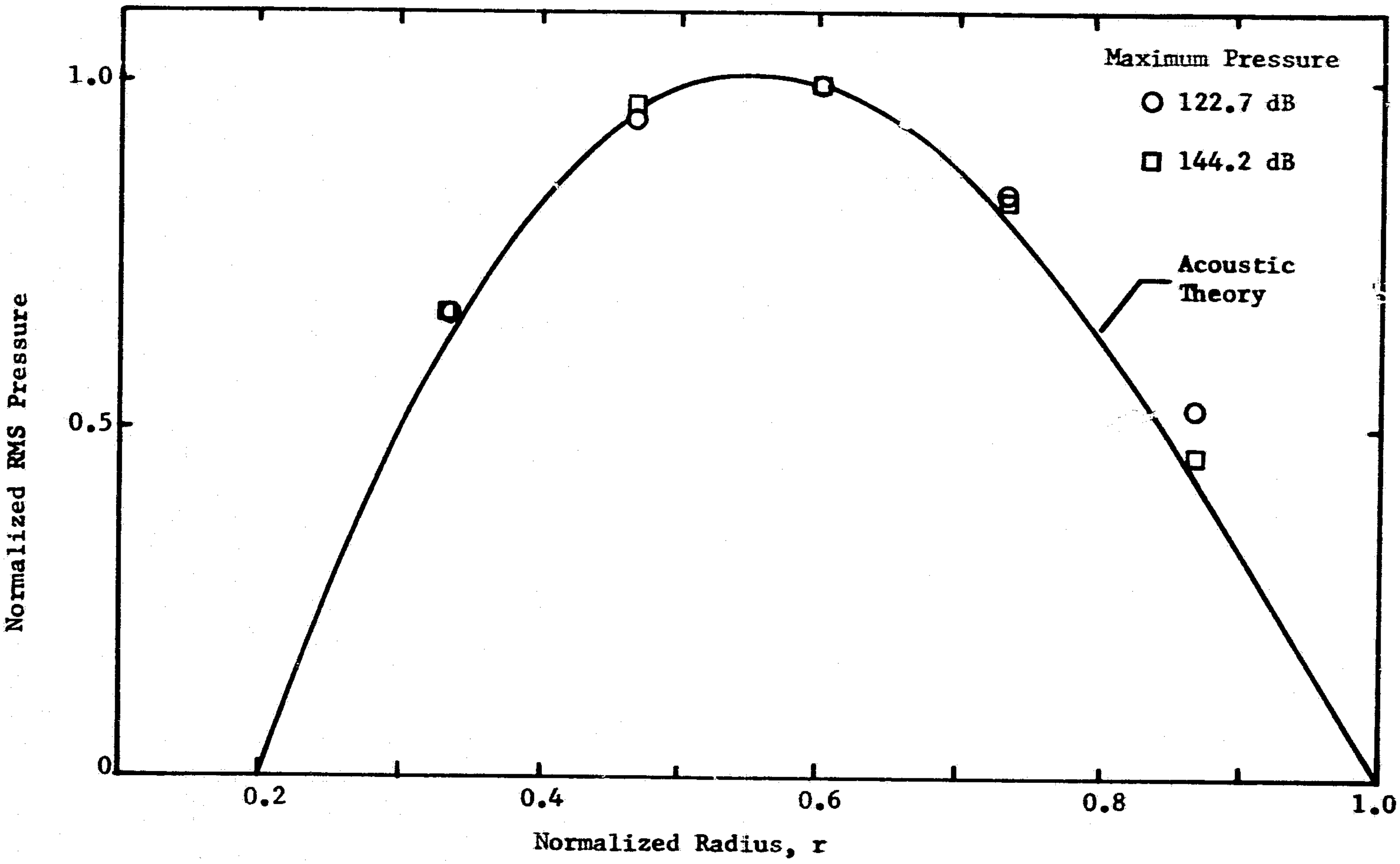

Figure 18. Radial Distribution of Oscillatory Pressure. 4 Drivers.

Figure 19 presents radial distributions of the difference between the mean or steady component of pressure, $\bar{p}$, and the ambient pressure, p_o. These time-averaged pressure differentials were measured using a slow-response (i.e., high volume) pressure transducer. The five data points in the central region of the cavity from $r = 0.35$ to $r = 0.85$ were measured using the static pressure taps labeled P_1 through P_5 in Figure 14. The two data points indicated by the triangular symbols were measured at the open boundaries ($r = 0.2$ and $r = 1.0$) using a 0.15 cm static pressure probe. These are the only data that indicate negative pressures. The accuracy of these two data points is questionable since crossflow over the probe due either to oscillatory motion or boundary layer streaming would reduce the pressure readings. Thus, the actual pressure at these open boundaries may be slightly higher than that indicated by these data points. Regardless, the mean pressures at the boundaries are nearly ambient.

In the upper portion of Figure 19 the pressure differentials are normalized by the amplitude of the oscillatory pressure, p' , measured at $r = 0.6$ (i.e., nearly the maximum value of the oscillatory pressure). In the lower portion the pressure differentials are normalized by the ambient pressure. Results are shown for the spinning wave driven both by 4 and 3 drivers. The reason for including the case of 3 drivers is that driver $D2_B$ is located along the radial line of the static pressure taps on the disc opposite these taps. It was thought that this driver might have a direct effect upon the pressures and, thus, driver $D2_B$ was not used in the tests with 3 drivers. As shown by the results of Figure 19, driver $D2_B$ does significantly change the pressure magnitudes, but it does not change the qualitative nature of the

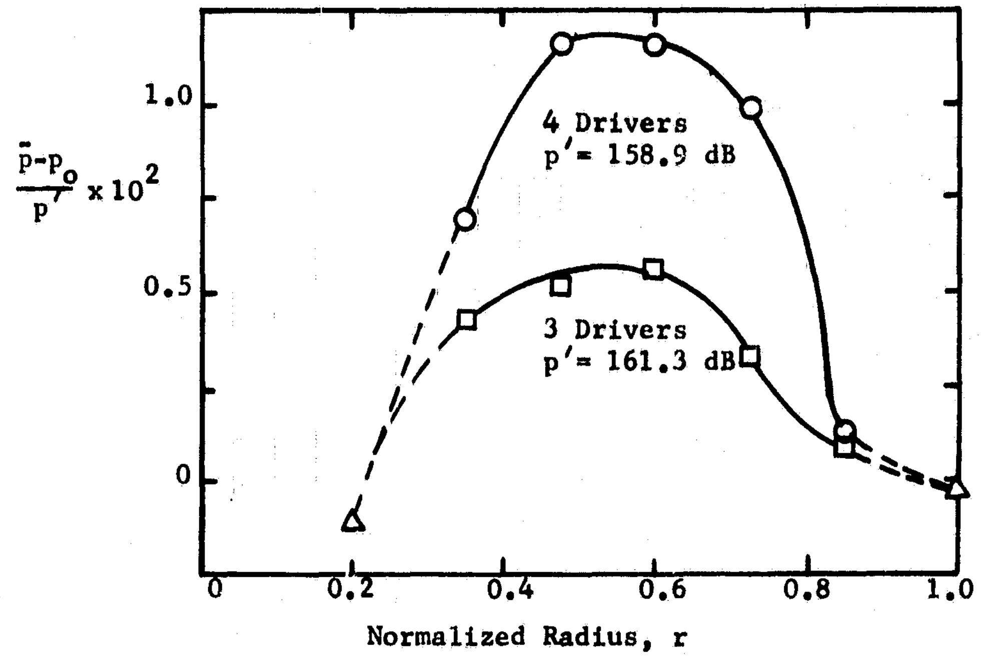

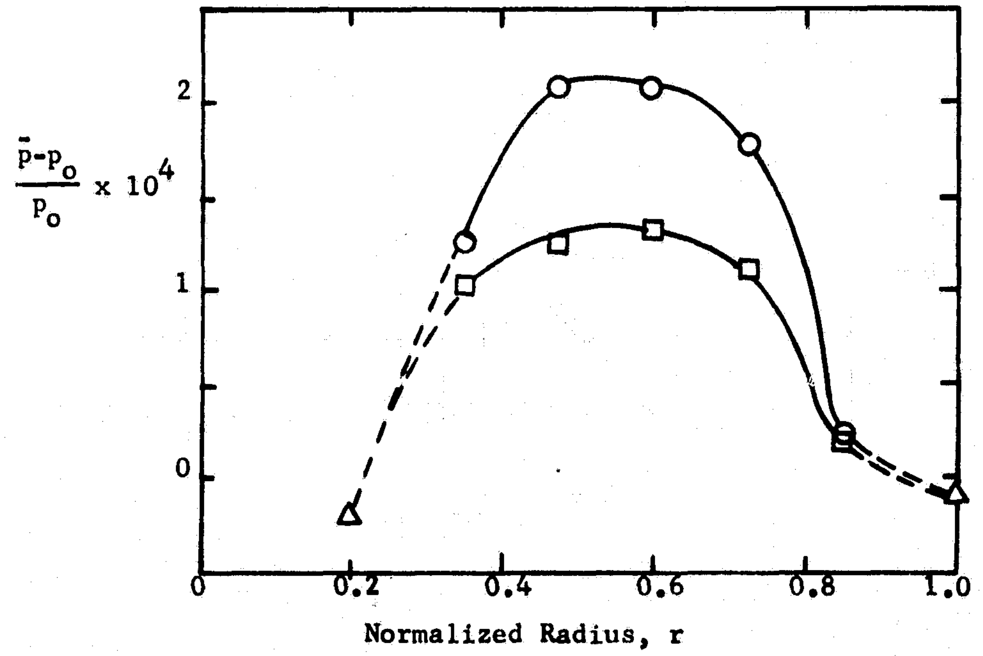

Figure 19. Radial Distribution of Mean Pressure.

data.

There are two important points to be made concerning the results of Figure 19. First, the oscillatory motion associated with the spinning wave is accompanied by a radial distribution of mean pressure. The theory also predicts a steady component of pressure superimposed on the oscillatory pressure. The magnitudes of the theoretical values of the steady component of pressure (i.e., $(\bar{p} - p_o)/p_o = -\gamma P_{23} \epsilon^2$) on the boundaries at $r = 0.2$ and $r = 1.0$ are about the same as the maximum value within the cavity (see Figure 7). Also the theory predicts that the steady component of pressure is greater than ambient near the mean radius, less than ambient at the open boundaries, and equal to ambient at about $r = 0.38$ and $r = 0.78$. However, in contrast, the experimental results show that the mean pressure is greater than ambient for the entire cavity except perhaps very near the open boundaries where it may be slightly less than ambient. The second point is that the pressure differential $\bar{p} - p_o$ is small in comparison with the amplitude of the oscillatory pressure p'. As shown by the upper portion of Figure 19, the ratio of these pressures is of the order of 10^{-2}. The value of the theoretical amplitude parameter ϵ for these tests was of the order of 10^{-2} also. Therefore, since p' arises as a first order term, $\bar{p} - p_o$ must enter as a second order term. This is as predicted by the theory which shows that the steady component of pressure first arises as a second order term. The amplitude parameter based on $p' = 161.3$ dB for the tests with 3 drivers is about $\epsilon = 0.03$. Using this in the second order theory (i.e., in the equation $(\bar{p} - p_o)/p_o = -\gamma P_{23} \epsilon^2$) yields a maximum theoretical value of $(\bar{p} - p_o)/p_o = 0.9 \times 10^{-4}$. This is in fair agreement, but slightly lower than, the maximum value of 1.25×10^{-4} for the corresponding results in the lower portion of Figure 19.

Hot Wire Results

The response of a hot wire in oscillatory flows and the experimental methods used in obtaining the hot-wire data will be considered first to aid in understanding and interpreting the hot-wire results. Figure 20 shows idealized responses of a hot wire in oscillatory flows. Figure 20a presents the case for a pure sinusoidal motion with zero mean flow velocity. The flow velocity u for one cycle of motion is shown in the upper plot. The lower plot shows the corresponding velocity u_w that would be measured by a hot wire assuming a faithful, quasi-steady response to the flow. For all results reported herein, this represents the idealized output voltage since the anemometer signals were linearized and scaled by the analogue circuitry so that the output signal was equal to the velocity in accordance with a steady flow calibration. Because the hot wire is insensitive to flow direction the hot wire yields a rectification of the actual velocity curve, as shown in the figure. This gives rise to an apparent mean velocity $\bar{u}_w$ which can be evaluated as the average or DC component of the output voltage.

Figure 20b presents the case in which a mean flow velocity $\bar{u}$ is superimposed upon the oscillatory velocity. The rectified signal from the hot wire is altered so that the maximum velocity for the two half-waves, u_{w1} and u_{w2}, and the half-wave lengths, λ_1 and λ_2, are now different. Furthermore, the indicated mean velocity $\bar{u}_w$ and the RMS value of the AC component of the output signal change with $\bar{u}$. For this case the mean flow

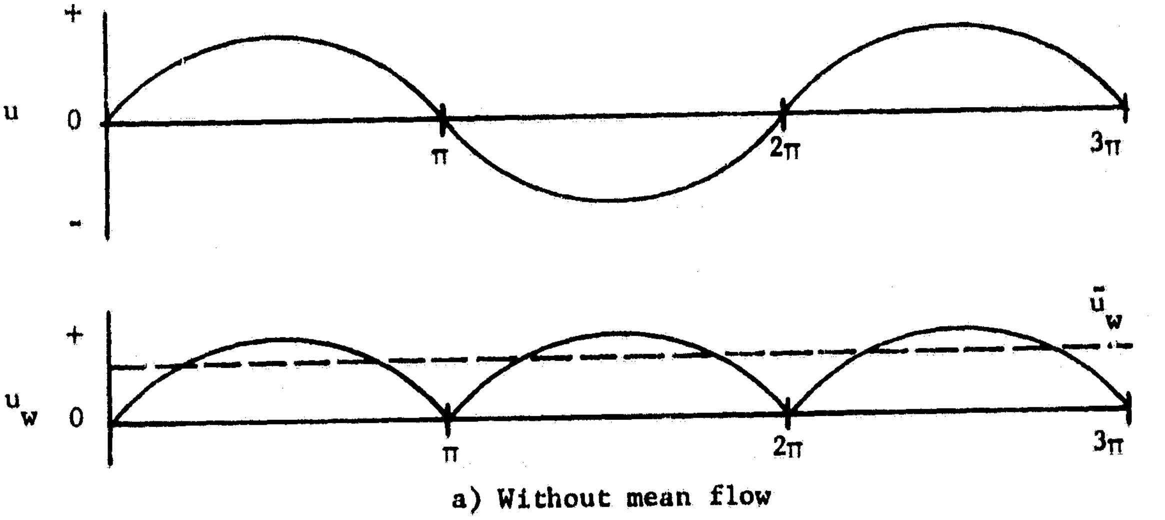

a) Without mean flow

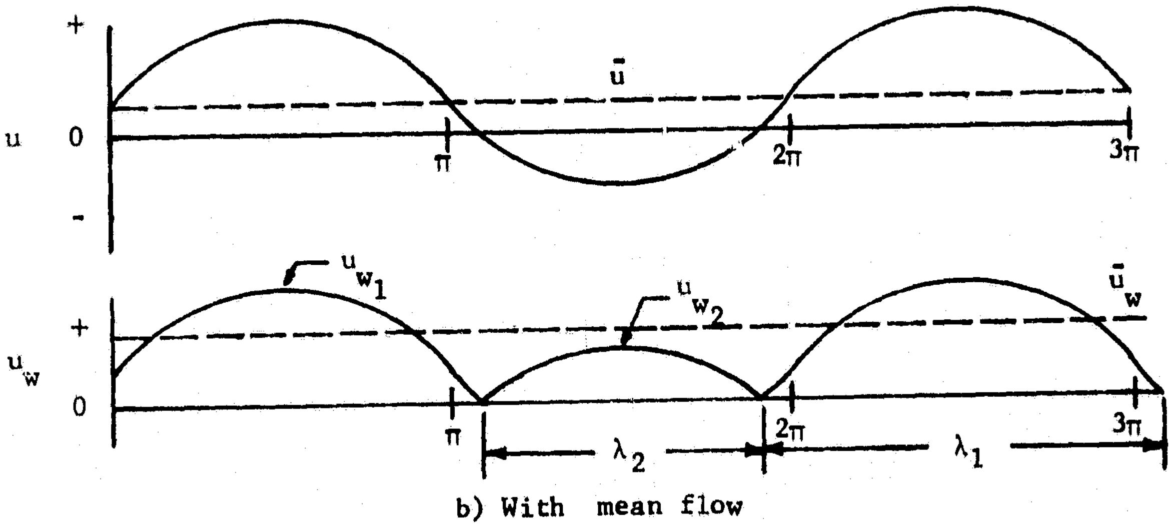

b) With mean flow

Figure 20. Idealized Hot-Wire Response.

velocity is given by

$$\bar{u} = (u_{w1} - w_{w2})/2$$

Also, it can be shown that $\bar{u}$ is determined by $\bar{u}_w$ and the RMS value of the AC component of the output signal. As will be shown later, the hot wire does not reproduce the rectified velocity curve. Apparently the quasi-steady condition is not sufficiently valid and, thus, the output signal is distorted, particularly during the time period near flow reversal when flow conditions change most rapidly. Nevertheless, asymmetries in the output signal like that shown in Figure 20b is a useful measure of the existence of a mean flow.

The asymmetries shown in Figure 20b reveal the existence of a mean flow velocity but not the mean flow direction. For the tests reported herein the mean flow direction is determined by the phases between the hot wire and microphone signals. This is illustrated in Figure 21 which considers the signals from microphone M2 and the hot wire at location W1. For this presentation it is assumed that the wave spins clockwise in the orientation of Figure 14. Also note that W1 is located 90^o clockwise from M2. Figure 21a shows the time-dependent output voltage E for M2. This represents a reference trace for the lower plots. Figure 21b shows the pressures at M2 corresponding to the microphone output trace. Because of the electronics the pressure is 180^o out of phase with the microphone output. The radial component of velocity, u_a, at the inner open boundary ($r = a$) and at the

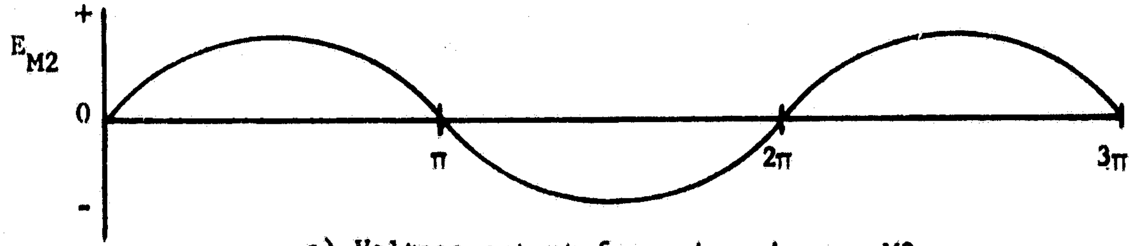

a) Voltage output from microphone M2

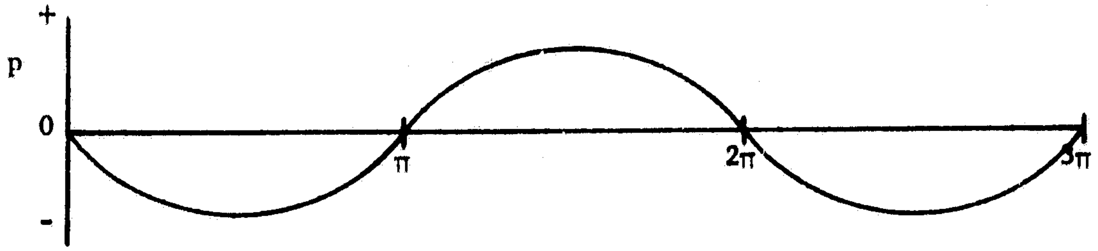

b) Alternating pressure component at M2

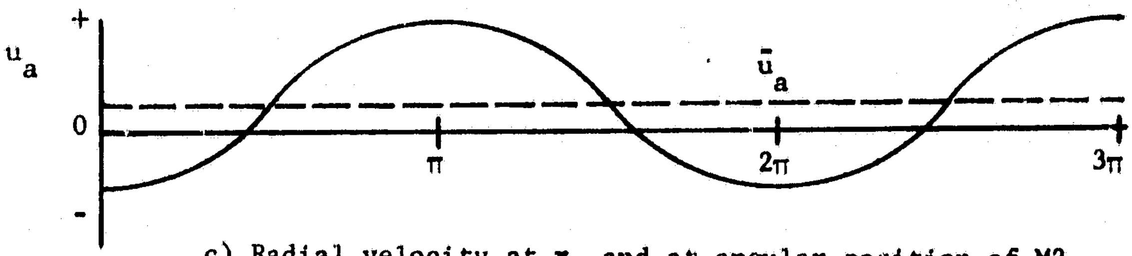

c) Radial velocity at r_a and at angular position of M2

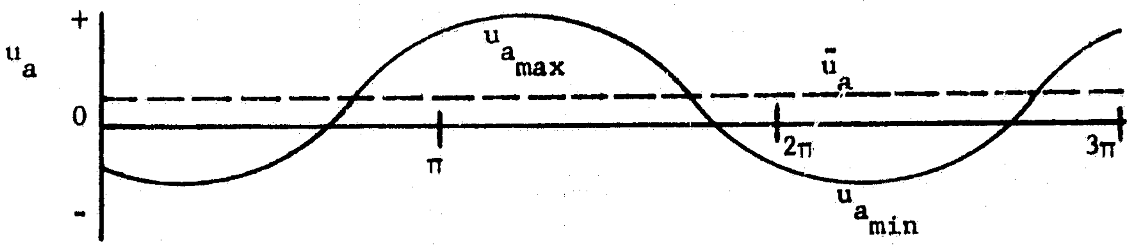

d) Radial velocity at r_a and at angular position of W1

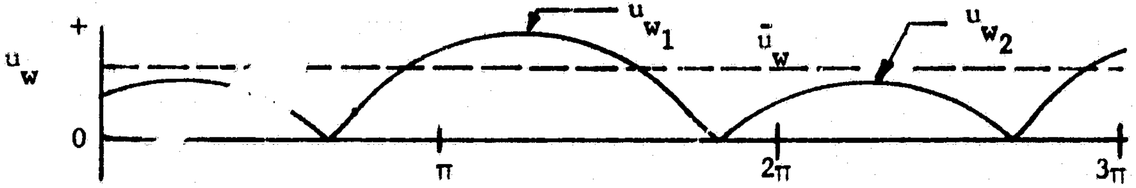

e) Idealized response of hot wire at location W1

Figure 21. Illustration of the Relation between Microphone Output and Hot-Wire Response.

angular position of M2 is shown in Figure 21c. This velocity wave as shown leads the pressure wave of Figure 21b in accordance with theory. For the sake of illustration, it is assumed also that the oscillatory velocity is superimposed upon a positive mean flow velocity (i.e., there is a net inflow rate at $r = a$). Since the wire location W1 is displaced 90^{o} in the spinning direction from M1, the oscillatory velocity u_a at W1 lags that of Figure 21c by 90^{o}. Figure 21d shows u_a at location W1. Finally, Figure 21e presents the rectification of this velocity at W1 and, thus, the idealized response of the hot wire. The important point of this illustration is the relation between the measurable hot wire and microphone signals which can be displayed simultaneously on an oscilloscope. As shown for this case of inflow at $r = a$ the phase lag between the maximum velocity u_{W1} and the maximum microphone output E_m is 135^{o} $(3\pi/2)$. The corresponding phase lags for the hot wire located at W2 or W3 are 180^{o} and 225^{o}, respectively. On the other hand, if the mean flow velocity $\bar{u}_a$ was negative each of these phase angles would change by 180^{o} since the locations of u_{W1} and u_{W2} would be interchanged. Thus, the phase between E_m and u_{W1} can be used to establish whether $\bar{u}_a$ is positive or negative.

A typical set of oscilloscope traces from the spinning wave tests is shown in Figure 22. Operation is with all four drivers at the fundamental frequency of 693 Hz. Because the camera was set for a shutter speed of 0.1 sec each trace shown on these photographs represent the superpositioning of about 70 sweeps across the oscilloscope trace. Since the band widths of the superimposed traces are small the signals are stationary. Figure 22a provides

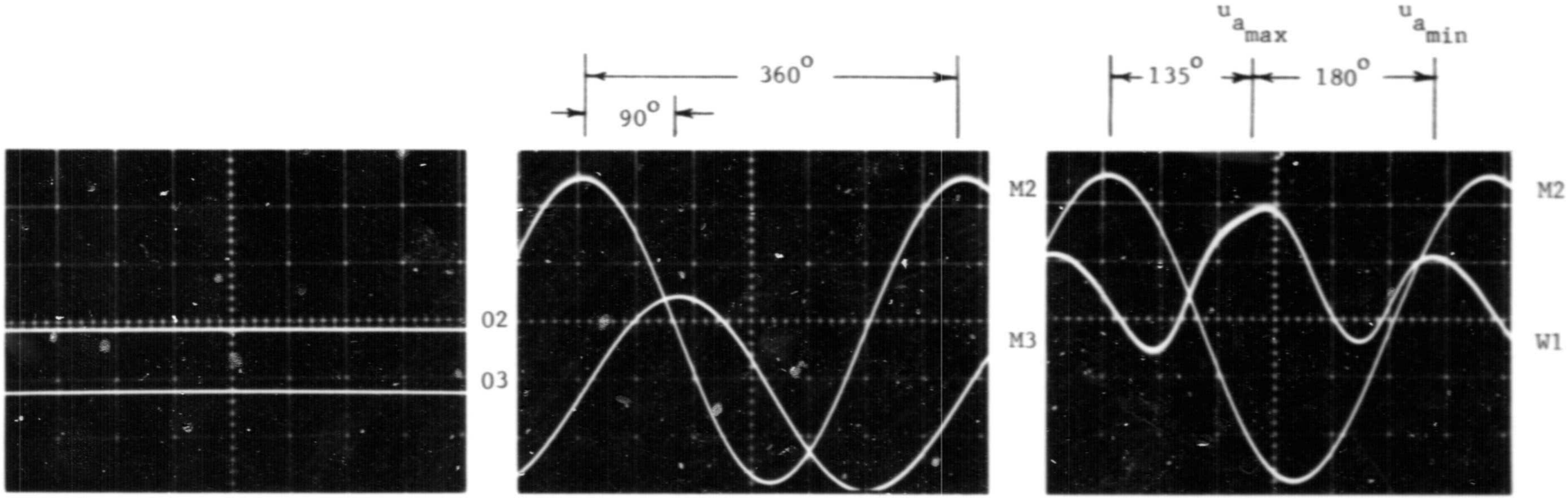

a. Zero reference traces

b. Microphone output traces

c. Microphone and hot-wire output traces

Figure 22. Typical Set of Oscilloscope Traces. f = 693 Hz. Hot Wire at W1.

the zero voltage references for the two channels. Figure 22b shows the simultaneous traces of the output signals from microphones M2 and M3 which have zero reference traces 02 and 03, respectively. This shows that the wave spins clockwise from M2 to M3 with the proper phase lag of 90° from M2 to M3. Figure 22c shows the simultaneous traces for M2 and the hot wire located at W1. This corresponds to the case depicted in Figure 21. The zero references for M2 and W1 are 02 and 03, respectively. Note first that the hot wire signals are always positive and, thus, present a rectification of the flow velocities. However, the minimum indicated velocity is not zero and, in contrast with the idealized response shown in Figure 21e, the valleys in the traces are well rounded. This is attributed to the failure of the quasi-steady flow calibration for these regions where the velocities change most rapidly and flow reversal occurs (during flow reversal the wake flows back across the wire). The important point from these results is that the successive peaks in the hot-wire traces are different, indicating a mean flow velocity superimposed on the oscillatory flow. Furthermore, the maximum voltage signal from the hot wire lags the maximum value of the microphone signal by about 135° indicating a net inflow as discussed in the previous paragraph. For reference, the locations for $u_{a_{max}}$ and $u_{a_{min}}$ based on the microphone trace are shown on the figure.

Figure 23 presents simultaneous traces of the output signals from M2 and the hot wire for all six hot wire locations. The zero voltage references are the same as in Figure 22a. The upper row of traces is for the hot wire on

ORIGINAL PAGE
BLACK AND WHITE PHOTOGRAPH

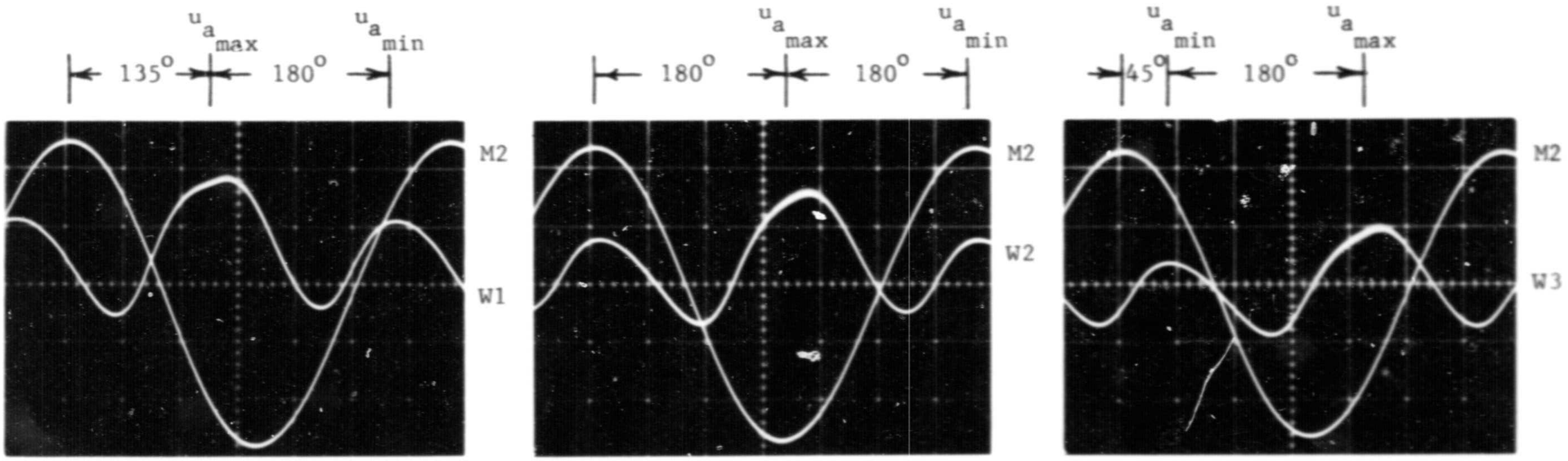

a. Hot wire at W1

b. Hot wire at W2

c. Hot wire at W3

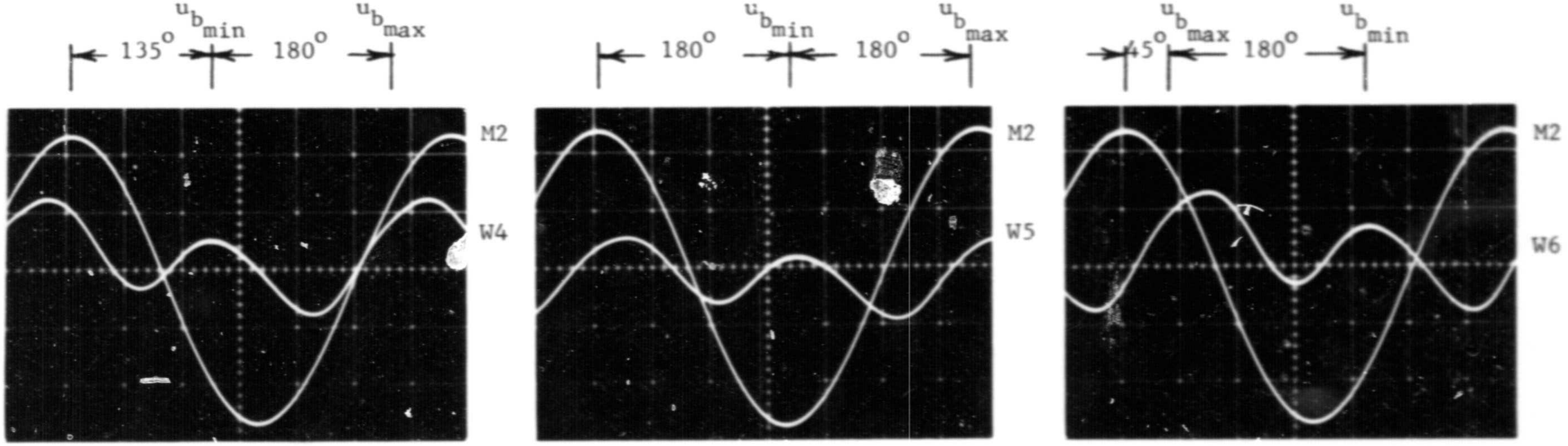

d. Hot wire at W4

e. Hot wire at W5

f. Hot wire at W6

Figure 23. Microphone and Hot-Wire Traces at 6 Hot-Wire Locations. f = 693 Hz.

the inner boundary $r = a$ and the lower row presents corresponding traces for the outer boundary $r = b$. Figure 23a is a repeat of Figure 22c. The locations of $u_{a_{max}}$ and $u_{a_{min}}$ and of $u_{b_{max}}$ and $u_{b_{min}}$ are displaced in increments of 45^o corresponding to the 45^o increments between hot-wire locations, as discussed earlier. As shown by the upper row of traces the hot-wire output is in phase with the radial velocity component and there is a net inflow rate at each location on the inner open boundary. The radial velocity components at the outer open boundary is 180^o out of phase with that at the inner boundary and, thus, the locations of the maximum and minimum velocities for the lower row of traces are interchanged with respect to those of the upper rows. But the hot-wire signals have also changed so that the maximum and minimum hot-wire outputs occur around $u_{b_{max}}$ and $u_{b_{min}}$, respectively. Since $u_{b_{max}}$ corresponds to outflow these traces show that there is a net mass outflow rate at the outer open boundary. The important point is that these results are consistent and show that flow is pumped through the cavity by the spinning wave and that the mean flow is radially outward from the inner open boundary to the outer open boundary.

Additional hot-wire measurements were obtained with the standing wave mode of operation driven using D1A and D2B (180^o out of phase with D1A). These results were simply recorded from the oscilloscope screen and not photographically documented. The results were as expected and consistent with those for the spinning wave mode. Along the radial line through D1A the hot-wire signals indicated a mean flow from the inner boundary at W1 to the outer boundary at W4. The mean flow rate decreased as the wire location was rotated around the periphery to W2 and W5. Finally, along the radial line normal to that through the drivers (i.e., at W3 and W6), where there must be a pressure node, there was no measurable hot-wire signal.

Results extracted from the photographs of Figure 23 were used to compute the maximum and minimum flow velocities, u_{W1} and u_{W2}, and the mean flow velocity as given by

$$\bar{u} = (u_{W1} - u_{W2})/2.$$

The results are based on the steady flow calibration of velocity versus voltage output and, thus, assume quasi-steady flow over the wire during the measurements of u_{W_1} and u_{W_2}. The velocities were obtained by measuring the displacements of the hot-wire traces from the zero reference traces and then applying a calibration factor for the oscilloscope deflection which was acquired from a separate test. The results are tabulated in part a) of Table 1. For these results the wire was located midway between the upper and lower disc at $y = 0$ (see the sketch at the bottom of Table 1) and the mean of the RMS pressures measured by M2 and M3 was 155.3 dB. This was about the highest possible power level without driver induced distortions. As shown in the table, the average values of $\bar{u}$ at the inner and outer open boundaries are 0.34 and 0.13 m/s. These are very small for this low power level. Each of these is about 15% of the corresponding amplitude of the oscillatory velocity evaluated as $(u_{W_1} + u_{W_2})/2$ and also listed in the table.

Table 1. Hot-Wire Results, f = 693 Hz.

a) y = 0

Wire Location	p RMS dB	u_{W_1} m/s	u_{W_2} m/s	$\bar{u}$ m/s	$\frac{u_{W_1}+u_{W_2}}{2}$ m/s	u_W RMS m/s	$\bar{u}_W$ m/s
W1	155.3	2.9	2.2	0.36	2.6	0.72	1.7
W2	155.3	2.7	1.9	0.39	2.3	0.62	1.5
W3	155.3	2.1	1.5	0.27	1.8	0.70	1.7
Averages		2.6	1.9	0.34	2.2		
W4	155.3	1.1	0.80	0.16	0.97	0.24	0.66
W5	155.3	0.81	0.66	0.08	0.73	0.19	0.57
W6	155.3	1.2	0.88	0.15	1.03	0.30	0.72
Averages		1.0	0.78	0.13	0.91		

b) Wire Location W1

y cm	p RMS dB	u_{W_1} m/s	u_{W_2} m/s	$\bar{u}$ m/s	$\frac{u_{W_1}+u_{W_2}}{2}$ m/s	u_W RMS m/s	$\bar{u}_W$ m/s
-0.5	155.3	3.3	2.5	0.43	2.9	0.82	2.0
0	155.3	2.9	2.2	0.36	2.6	0.72	1.7
0.5	155.3	2.9	2.1	0.41	2.5	0.79	1.9
0.9	155.3	≈ 1.7	≈ 1.7	≈ 0	≈ 1.7	0.52	1.3

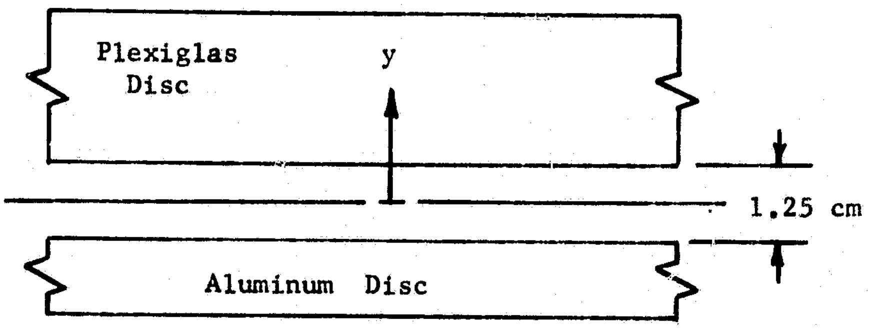

The amplitude parameter ϵ is about 0.02 for these tests at the RMS pressure of 155.3 dB. This indicates that the acoustic solution should be a good approximation for these test conditions. However, the amplitudes of the oscillatory velocity at the inner and outer open boundaries as predicted by the acoustic solution for 155.3 dB at the pressure antinode are 6.0 and 3.1 m/s. These are about a factor of three higher than the mean values of 2.2 and 0.91 m/s listed in the table. Also, it is important to point out that the ratio of $\bar{u}$ at the inner and outer boundaries is about 2.5 whereas the flow area ratio is 5. These differences cannot be explained, but perhaps are due to a combination of things such as inadequacy of the steady flow hot wire calibration, asymmetries, and viscous effects. Nevertheless, it is felt that the qualitative behavior is correctly represented. The mean velocity $\bar{u}_W$ and the RMS value of u_W are listed in Table 1a also since they were evaluated separately from the oscilloscope data using an integrating voltmeter and a true RMS meter. These data are entirely consistent with those obtained from the oscilloscope traces.

Part b) of Table 2 tabulates results for the hot wire at W1 and four values of y. The corresponding photographs of the oscilloscope traces are shown in Figure 23c, for y = 0, and Figure 24, for y = ± 0.5 and y = 0.9 cm. For the three locations within the 1.25 cm gap (i.e., y = 0 and y = ± 0.5 cm) the velocities are essentially the same. At y = ± 0.5 cm the band width of the superimposed traces has increased very slightly relative to that at y = 0. At y = 0.9 the wire is located outside the gap and the oscillatory signal is not stationary as evidenced by the multiple traces. However, it appears that on

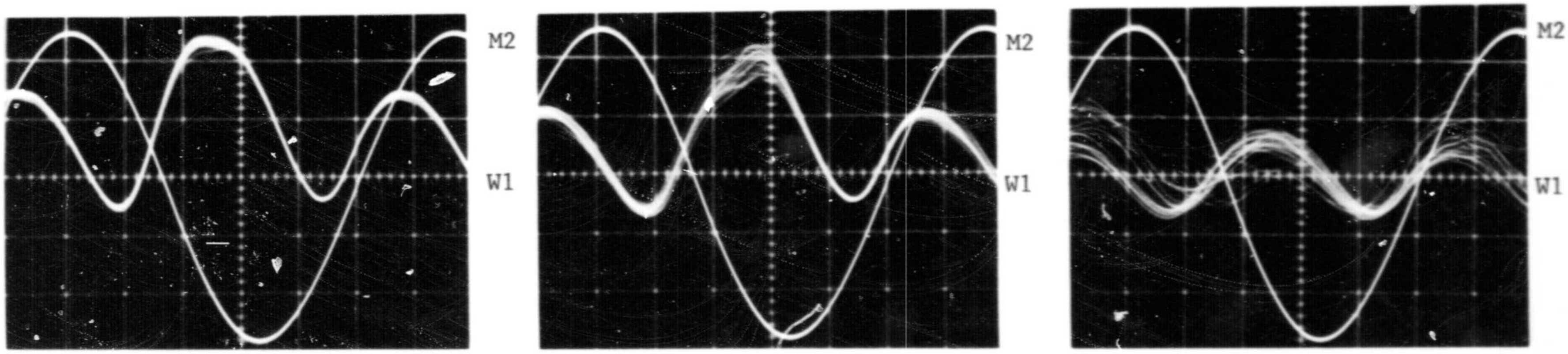

a. y = - 0.5 cm

b. y = 0.5 cm

c. y = 0.9 cm

Figure 24. Microphone and Hot-Wire Traces for Hot-Wire Location W1 at Different Lateral Positions.
f = 693 Hz.

the average the peaks and valleys in the traces are the same and, thus, there is oscillation with no mean flow.

Flow Visualization

Flow visualization was employed to support the hot wire predictions of a mean flow radially outward through the cavity. Smoke and a tufted wand were used. A very sensitive tufted wand constructed with very fine strands of fiberglas showed without question that there was inflow around the complete periphery of the inner open boundary. Outflow was indicated at the outer boundary but, because of the very low velocities superimposed on the oscillatory motion, these results were not so conclusive.

It was not possible to use a steady flow smoke trail to visualize the flow since the velocity of the smoke source was significant compared with the mean flow velocity. However, prior to starting oscillations it was possible to fill the cavity with smoke which becomes stationary and diffuses very slowly. Thus, the cavity could be filled with smoke and, after a short settling time, the driver quickly excited to produce the spinning wave. Tests of this type showed that the smoke was rapidly exhausted through the outer open boundary once the spinning wave was excited. Thus again the existence of a mean flow from the center outward was verified.

CONCLUDING REMARKS

In order to assess the feasibility of the spinning wave engine concept, the acoustics of an annular cavity was investigated using a theoretical analysis and an experimental model. The primary objective of the investigation was to determine whether a spinning wave excited in the cavity could pump flow through the cavity, which was bounded on the sides by two parallel discs and open to the environment at the inner and outer peripheries.

The theoretical analysis developed under this project was an extension of the nonlinear analysis of Maslen and Moore to study the case of an annular pancake cavity with open boundaries. This analysis involves a perturbation scheme in which the velocity potential and pressure are expanded in terms of an amplitude parameter. Solutions were obtained to third order in this amplitude parameter. These solutions yielded a steady contribution to the pressure perturbation which was second order in the amplitude parameter and did not vanish at the inner and outer boundaries as required by the open boundary conditions. Furthermore the analysis did not predict a corresponding steady velocity component; that is, the analysis could not predict the acoustic pumping of flow through the cavity.

The spinning wave engine concept has been tested experimentally using acoustic drivers to excite oscillatory motion in an annular cavity. The spinning wave was achieved by superimposing orthogonal standing waves driven 90° out of phase. The major thrust of the experiments was to determine if the spinning wave pumped flow through the cavity. Also some tests were made to assess the theory.

Simultaneous measurements of hot wire and microphone responses have shown that the spinning wave pumps a mean flow radially outward through the cavity. This conclusion has been verified by flow visualization using both a sensitive tufted wand and smoke as flow tracers. Measured radial distributions of the amplitude of periodic pressures were in good agreement with the theoretical predictions. Also, the experiments showed that the spinning wave gives rise to a radial distribution of mean pressure which is of second order, as predicted by the theory. In contrast with the theory, however, the measurements indicated that these mean pressures were positive throughout the entire cavity. Furthermore, the experimental value of the fundamental frequency was about 10 percent below that predicted by the theory. Perhaps these discrepancies between theory and test results are associated with the difficulties encountered in satisfying the boundary conditions with the theory.

To further evaluate the potential of the spinning wave engine, tests at higher power levels are needed. Because of driver limitations, the results reported herein were essentially at the acoustic level. In fact, the maximum value of the amplitude parameter was about 0.025. Furthermore, the accuracy of mean flow velocities measured by hot wires in such a flow field which is dominated by oscillatory motion is open to question. Thus, for accurate mean velocity data additional hot wire calibration tests are needed or the velocities must be measured by a more reliable instrument such as a laser velocimeter.

In spite of the limitations of the theoretical analysis and the experimental measurements, the primary objective of this research project has been met. The experimental detection of a radial mean flow driven by the spinning wave at relatively low acoustic amplitudes has demonstrated the feasibility of the spinning wave engine concept. It is anticipated that this acoustic pumping will increase as the square of the acoustic amplitude giving much larger mean flow velocities at the larger acoustic amplitudes expected in a spinning wave engine. Thus further development and testing of the spinning wave engine concept is definitely warranted.

Appendix A

Solution for Second Order Function $f(\alpha)$

The second order function $f(\alpha)$ is described by the inhomogeneous second order differential equation:

$$f''(\alpha) + \frac{1}{\alpha} f'(\alpha) + 4\left(1 - \frac{n^2}{\alpha^2}\right) f(\alpha) = R_n^2(\alpha) \qquad \text{(A-1)}$$

where $R_n(\alpha)$ is given by Eq. (7). Inspection of this equation reveals that the change of variable $z = 2\alpha$ will transform this equation to a Bessel equation. Thus Eq. (A-1) becomes:

$$\frac{d^2f}{dz^2} + \frac{1}{z}\frac{df}{dz} + \left[1 - \frac{(2n)^2}{z^2}\right] f = R_n^2(z/2) \qquad \text{(A-2)}$$

The homogeneous version of Eq. (A-2) has the general solution:

$$f_h(z) = C_1 J_{2n}(z) + C_2 Y_{2n}(z)$$

which implies that the homogeneous solution of the original equation (Eq. (A-1)) is given by:

$$f_h(\alpha) = C_1 J_{2n}(2\alpha) + C_2 Y_{2n}(2\alpha) \qquad \text{(A-3)}$$

The complete solution is the sum of the solution of the homogeneous equation $f_h(\alpha)$ given by Eq. (A-3) and the particular solution $f_p(\alpha)$. Thus

Thus the general solution of Eq. (A-1) can be written as follows:(5)

$$f(\alpha) = J_{2n}(2\alpha)\left[C_1 - \int \frac{Y_{2n}(2\alpha)\ R_n^2(\alpha)\ d\alpha}{W(\alpha)}\right]$$

$$+ Y_{2n}(2\alpha)\left[C_2 + \int \frac{J_{2n}(2\alpha)\ R_n^2(\alpha)\ d\alpha}{W(\alpha)}\right] \qquad \text{(A-4)}$$

where $W(\alpha)$ is the Wronskian given by

$$W(\alpha) = 2J_{2n}(2\alpha)\,Y'_{2n}(2\alpha) - 2Y_{2n}(2\alpha)\,J'_{2n}(2\alpha) \qquad \text{(A-5)}$$

and primes denote differentiation with respect to the argument.

The indefinite integrals in Eq. (A-4) may be replaced by definite integrals by making a suitable adjustment in the constants C_1 and C_2. Choosing the lower limit of integration at the inner boundary $\alpha = \nu\beta_o$, the general solution becomes:

$$f(\alpha) = \left[C_1 - K_2(\alpha)\right] J_{2n}(2\alpha) + \left[C_2 + K_1(\alpha)\right] Y_{2n}(2\alpha) \qquad \text{(A-6)}$$

where

$$K_1(\alpha) = \int_{\nu\beta_o}^{\alpha} \frac{J_{2n}(2x)\ R_n^2(x)\ dx}{W(x)} \qquad \text{(A-7)}$$

$$K_2(\alpha) = \int_{\nu\beta_o}^{\alpha} \frac{Y_{2n}(2x)\ R_n^2(x)\ dx}{W(x)} \qquad \text{(A-8)}$$

The unknown constants C_1 and C_2 are determined from the boundary conditions imposed upon $f(\alpha)$ as given by Eqs. (31). Applying the boundary condition at $\alpha = \nu\beta_o$ gives:

$$C_1 J_{2n}(2\nu\beta_o) + C_2 Y_{2n}(2\nu\beta_o) = \frac{-1}{4(\gamma+1)}\left[R_n'(\nu\beta_o)\right]^2 \qquad \text{(A-9)}$$

since $K_1(\nu\beta_o) = K_2(\nu\beta_o) = 0$ from Eqs. (A-7) and (A-8). The boundary condition at $\alpha = \beta_o$ gives:

$$C_1 J_{2n}(2\beta_o) + C_2 Y_{2n}(2\beta_o) = \frac{-1}{4(\gamma+1)}\left[R_n'(\beta_o)\right]^2 + K_2(\beta_o) J_{2n}(2\beta_o) - K_1(\beta_o) Y_{2n}(2\beta_o) \qquad \text{(A-10)}$$

Solving Eq. (A-9) for C_2 gives:

$$C_2 = \frac{\frac{-1}{4(\gamma+1)}\left[R_n'(\nu\beta_o)\right]^2 - C_1 J_{2n}(2\nu\beta_o)}{Y_{2n}(2\nu\beta_o)} \qquad \text{(A-11)}$$

Substituting Eq. (A-11) into Eq. (A-10) and solving for C_1 then yields:

$$C_1 = \left[-\frac{1}{4(\gamma+1)}\left\{Y_{2n}(2\nu\beta_o)\left[R_n'(\beta_o)\right]^2 - Y_{2n}(2\beta_o)\left[R_n'(\nu\beta_o)\right]^2\right\} - Y_{2n}(2\nu\beta_o) f_p(\beta_o)\right] \Big/ \left[J_{2n}(2\beta_o)\, Y_{2n}(2\nu\beta_o) - J_{2n}(2\nu\beta_o) Y_{2n}(2\beta_o)\right] \qquad \text{(A-12)}$$

where $f_p(\beta_o) = K_1(\beta_o)\,Y_{2n}(2\beta_o) - K_2(\beta_o)J_{2n}(2\beta_o)$

For given values of γ, ν and n (tangential mode number), the eigenvalue β_o is readily determined and the quantities appearing in Eqs. (A-11) and (A-12) can be calculated. Equation (A-12) is first evaluated to obtain C_1 which is then substituted into Eq. (A-11) to obtain C_2. For $\nu = 0.2$, $\gamma = 1.4$ and $\beta_o = 4.23575$, the constants of integration become $C_1 = -0.36495$ and $C_2 = -0.04275$.

Once the constants of integration are obtained, Eq. (A-6) is used to calculate $f(\alpha)$. In this process, a numerical integration technique must be used to evaluate $K_1(\alpha)$ and $K_2(\alpha)$.

In computing the third order quantities, the derivative $f'(\alpha)$ is also needed. Differentiating Eq. (A-6) gives:

$$f'(\alpha) = 2\left[C_1 - K_2(\alpha)\right] J'_{2n}(2\alpha) + 2\left[C_2 + K_1(\alpha)\right] Y'_{2n}(2\alpha)$$

$$- K'_2(\alpha)J_{2n}(2\alpha) + K'_1(\alpha)Y_{2n}(2\alpha) \qquad \text{(A-13)}$$

where $K'_1(\alpha)$ and $K'_2(\alpha)$ are simply the integrands in Eqs. (A-7) and (A-8).

Appendix B

Solution for Third Order Functions F_1 and F_5

Solution for $F_1(\alpha)$

The third order function $F_1(\alpha)$ is described by the inhomogeneous second order differential equation:

$$F_1'' + \frac{1}{\alpha} F_1' + 9\left(1 - \frac{n^2}{\alpha^2}\right) F_1 = \mathcal{R}_1(\alpha) \qquad \text{(B-1)}$$

where

$$\mathcal{R}_1(\alpha) = \frac{1}{4} \Big\} \frac{1}{\alpha} (R_n')^3 + \left[13 + 5\left(\frac{\gamma - 1}{2}\right) + \frac{n^2}{\alpha^2}\right] R_n (R_n')^2$$

$$- \frac{n^2}{\alpha^3} R_n^2 R_n' - \left[\frac{n^4}{\alpha^4} + \left(12 + 5\left[\frac{\gamma - 1}{2}\right]\right) \frac{n^2}{\alpha^2} + (\gamma - 1)(\gamma + 5)\right] R_n^3$$

$$+ \left[12(\gamma + 1)\frac{n^2}{\alpha^2} + 6(\gamma^2 - 1)\right] R_n f - 6(\gamma + 1) R_n' f' \Big\{ \qquad \text{(B-2)}$$

The change of variable $z = 3\alpha$ will transform Eq. (B-1) into an inhomogeneous Bessel equation given by

$$\frac{d^2 F_1}{dz^2} + \frac{1}{z}\frac{dF_1}{dz} + \left[1 - \frac{(3n)^2}{z^2}\right] F_1 = \mathcal{R}_1(z/3) \qquad \text{(B-3)}$$

The homogeneous version of Eq. (B-3) has the general solution given by:

$$F_{1h}(z) = C_{11} J_{3n}(z) + C_{12} Y_{3n}(z)$$

and returning to the original variable α yields the homogeneous solution of the original equation as:

$$F_{1h}(\alpha) = C_{11} J_{3n}(3\alpha) + C_{12} Y_{3n}(3\alpha) \tag{B-4}$$

Adding to this the particular solution $F_{1p}(\alpha)$ yields the following solution of the inhomogeneous equation$^{(5)}$ (Eq. (B-2)):

$$\begin{aligned} F_1(\alpha) = {} & J_{3n}(3\alpha)\left[C_{11} - \int \frac{Y_{3n}(3\alpha)\,\mathcal{R}_1(\alpha)\,d\alpha}{W_1(\alpha)}\right] \\ & + Y_{3n}(3\alpha)\left[C_{12} + \int \frac{J_{3n}(3\alpha)\,\mathcal{R}_1(\alpha)\,d\alpha}{W_1(\alpha)}\right] \end{aligned} \tag{B-5}$$

where $W_1(\alpha)$ is the Wronskian given by:

$$W_1(\alpha) = 3J_{3n}(3\alpha)Y'_{3n}(3\alpha) - 3Y_{3n}(3\alpha)J'_{3n}(3\alpha) \tag{B-6}$$

and primes denote differentiation with respect to the argument.

Replacing the indefinite integrals in Eq. (B-5) with definite integrals and adjusting the constants of integration gives:

$$F_1(\alpha) = \left[C_{11} - I_{12}(\alpha)\right] J_{3n}(3\alpha) + \left[C_{12} + I_{11}(\alpha)\right] Y_{3n}(3\alpha) \tag{B-7}$$

where

$$I_{11}(\alpha) = \int_{\nu\beta_o}^{\alpha} \frac{J_{3n}(3x)\ \mathcal{R}_1(x)dx}{W_1(x)} \tag{B-8}$$

$$I_{12}(\alpha) = \int_{\nu\beta_o}^{\alpha} \frac{Y_{3n}(3x)\mathcal{R}_1(x)dx}{W_1(x)} \tag{B-9}$$

The constants C_{11} and C_{12} are obtained by applying the boundary conditions imposed upon $F_1(\alpha)$ as given by Eqs. (34). This yields the following equations to be solved for C_{11} and C_{12}:

$$C_{11}J_{3n}(3\nu\beta_o) + C_{12}Y_{3n}(3\nu\beta_o) = -\frac{1}{12}(\gamma+1)R_n'(\nu\beta_o)f'(\nu\beta_o) \tag{B-10}$$

$$C_{11}J_{3n}(3\beta_o) + C_{12}Y_{3n}(3\beta_o) = -\frac{1}{12}(\gamma+1)R_n'(\beta_o)f'(\beta_o)$$
$$+ I_{12}(\beta_o)J_{3n}(3\beta_o) - I_{11}(\beta_o)Y_{3n}(3\beta_o) \tag{B-11}$$

Solving Eq. (B-10) for C_{12} yields:

$$C_{12} = \frac{-\left(\frac{\gamma+1}{12}\right)R_n'(\nu\beta_o)f'(\nu\beta_o) - C_{11}J_{3n}(3\nu\beta_o)}{Y_{3n}(3\nu\beta_o)} \tag{B-12}$$

Substituting Eq. (B-12) into Eq. (B-11) and solving for C_{11} gives:

$$C_{11} = \left\{ -\left(\frac{\gamma+1}{12}\right)\left[R_n'(\beta_o)f'(\beta_o)Y_{3n}(3\nu\beta_o) - R_n'(\nu\beta_o)f(\nu\beta_o)Y_{3n}(3\beta_o)\right] - Y_{3n}(3\nu\beta_o)F_{1p}(\beta_o)\right\} \Big/ \left[J_{3n}(3\beta_o)Y_{3n}(3\nu\beta_o) - J_{3n}(3\nu\beta_o)Y_{3n}(3\beta_o)\right] \qquad \text{(B-13)}$$

where

$$F_{1p}(\beta_o) = I_{11}(\beta_o)Y_{3n}(3\beta_o) - I_{12}(\beta_o)J_{3n}(3\beta_o)$$

Once the parameters γ, ν and n are specified and the second order functions are computed, all of the quantities in Eqs. (B-12) can then be calculated. Equation (B-12) is first solved for C_{12} which is next substituted into Eq. (B-13) to obtain C_{11}. For $\nu = 0.2$, $\gamma = 1.4$ and $\beta_o = 4.23575$, the constants of integration become $C_{11} = 0.13464$ and $C_{12} = -0.01078$.

After the constants C_{11} and C_{12} are obtained, Eq. (B-7) is used to calculate $F_1(\alpha)$. The functions $I_{11}(\alpha)$ and $I_{12}(\alpha)$ are obtained by numerical integration.

In computing the radial velocity by Eq. (43) the derivative $F_1'(\alpha)$ is also needed. Differentiating Eq. (B-7) yields:

$$F_1'(\alpha) = 3\left[C_{11} - I_{12}(\alpha)\right]J_{3n}'(3\alpha) + 3\left[C_{12} + I_{11}(\alpha)\right]Y_{3n}'(3\alpha) - I_{12}'(\alpha)J_{3n}(3\alpha) + I_{11}'(\alpha)Y_{3n}(3\alpha) \qquad \text{(B-14)}$$

where $I'_{11}(\alpha)$ and $I'_{12}(\alpha)$ are simply the integrands in Eqs. (B-8) and (B-9).

Solution for β_2 and $F_5(\alpha)$

The third order function $F_5(\alpha)$ is described by the inhomogeneous Bessel equation:

$$F_5'' + \frac{1}{\alpha} F_5' + \left(1 - \frac{n^2}{\alpha^2}\right) F_5 = R_5(\alpha) \tag{B-15}$$

where

$$\begin{aligned} R_5(\alpha) = \frac{1}{4} \Big\} & - \frac{3}{\alpha}(R_n')^3 + \left[-7 + \frac{\gamma - 1}{2} + 5\frac{n^2}{\alpha^2}\right] R_n (R_n')^2 \\ & - \frac{n^2}{\alpha^3} R_n^2 R_n' - \left[\frac{n^4}{\alpha^4} + \left(4 + 5\left[\frac{\gamma - 1}{2}\right]\right) \frac{n^2}{\alpha^2} + (\gamma^2 - 1)\right] R_n^3 \\ & + \left[4(\gamma + 1) \frac{n^2}{\alpha^2} + 2(\gamma^2 - 1)\right] R_n f + 2(\gamma + 1) R_n' f' \Big\{ \end{aligned} \tag{B-16}$$

The general solution of the homogeneous equation is

$$F_{5h}(\alpha) = C_{51} J_n(\alpha) + C_{52} Y_n(\alpha) \tag{B-17}$$

Adding the particular solution to Eq. (B-17) yields the solution of the inhomogeneous equation as(5):

$$F_5(\alpha) = [C_{51} - I_{52}(\alpha)] J_n(\alpha) + [C_{52} + I_{51}(\alpha)] Y_n(\alpha) \tag{B-18}$$

where

$$I_{51}(\alpha) = \int_{\nu\beta_o}^{\alpha} \frac{J_n(x)\,\mathcal{R}_5(x)dx}{W_5(x)} \tag{B-19}$$

$$I_{52}(\alpha) = \int_{\nu\beta_o}^{\alpha} \frac{Y_n(x)\,\mathcal{R}_5(x)dx}{W_5(x)} \tag{B-20}$$

and $W_5(\alpha)$ is the Wronskian given by:

$$W_5(\alpha) = J_n(\alpha)Y_n'(\alpha) - Y_n(\alpha)J_n'(\alpha) \tag{B-21}$$

The constants of integration C_{51} and C_{52} must be determined using the boundary conditions given by Eqs. (35). Substituting Eq. (B-18) into Eqs. (35) yields:

$$C_{51}J_n(\nu\beta_o) + C_{52}Y_n(\nu\beta_o) = \left[-\frac{\gamma+1}{4}f'(\nu\beta_o) - \nu\beta_2\right]R_n'(\nu\beta_o) \tag{B-22}$$

$$C_{51}J_n(\beta_o) + C_{52}Y_n(\beta_o) = \left[\frac{\gamma+1}{4}\,f'(\beta_o) - \beta_2\right]R_n'(\beta_o)$$

$$+ I_{52}(\beta_o)J_n(\beta_o) - I_{51}(\beta_o)Y_n(\beta_o) \tag{B-23}$$

Unlike the corresponding equations obtained for $f(\alpha)$ and $F_1(\alpha)$, Eqs. (B-22) and (B-23) contain an additional unknown parameter, the second order eigenvalue correction β_2. Thus an additional relationship is needed to obtain β_2, C_{51} and C_{52}.

If β_2 were known, the right hand sides of Eqs. (B-22) and (B-23) could be calculated. Denoting these quantities by r_1 and r_2 we have:

$$\begin{aligned} J_n(\nu\beta_o)\,C_{51} + Y_n(\nu\beta_o)\,C_{52} &= r_1 \\ J_n(\beta_o)\,C_{51} + Y_n(\beta_o)\,C_{52} &= r_2 \end{aligned} \qquad \text{(B-24)}$$

This is a linear system of two equations in two unknowns which can be solved for C_{51} and C_{52} if the determinant of the system is nonzero. The determinant Δ is given by

$$\Delta = J_n(\nu\beta_o)Y_n(\beta_o) - Y_n(\nu\beta_o)J_n(\beta_o) \qquad \text{(B-25)}$$

Comparing Eq. (B-25) with Eq. (8), which was used to determine β_o, shows that $\Delta = 0$, since β_o is precisely the value that causes the right-hand-side of Eq. (B-25) to vanish. This implies that Eqs. (B-24) is either inconsistent (i.e., no solution exists) or that the system is indeterminate (i.e., infinitely many solutions exist). The condition $\Delta = 0$ also implies that

$$\frac{J_n(\nu\beta_o)}{J_n(\beta_o)} = \frac{Y_n(\nu\beta_o)}{Y_n(\beta_o)} \qquad \text{(B-26)}$$

and the system is indeterminate if r_1/r_2 is also this ratio, otherwise no solution exists. This provides a method of determining β_2 by requiring that solutions for C_{51} and C_{52} exist, thus we require that:

$$\frac{r_1}{r_2} = \frac{J_n(\nu\beta_o)}{J_n(\beta_o)}$$

or that

$$\frac{\left[\frac{\gamma+1}{4} f'(\nu\beta_o) - \nu\beta_2\right] R_n'(\nu\beta_o)}{\left[\frac{\gamma+1}{4} f'(\beta_o) - \beta_2\right] R_n'(\beta_o) - F_{5p}(\beta_o)} = \frac{J_n(\nu\beta_o)}{J_n(\beta_o)} \tag{B-27}$$

where

$$F_{5p}(\beta_o) = I_{51}(\beta_o)Y_n(\beta_o) - I_{52}(\beta_o)J_n(\beta_o) \tag{B-28}$$

Solving Eq. (B-27) for β_2 and introducing $\sigma = J_n(\beta_o)/J_n(\nu\beta_o)$ yields Eq. (36) which is used to calculate β_2.

With β_2 given by Eq. (36), Eqs. (B-22) and (B-23) become an indeterminate system; that is, there are infinitely many solutions for C_{51} and C_{52}. In order to obtain a unique solution for $F_5(\alpha)$, an additional relationship between C_{51} and C_{52} must be found. This can be done if one states more precisely what is meant by the amplitude parameter ϵ.

Until now, the amplitude parameter ϵ was used in the perturbation analysis only as an ordering parameter and was not precisely related to a physical quantity such as pressure amplitude. In order to relate the theoretical calculations to experimental measurements, a more precise definition of ϵ is needed. Since the Maslen and Moore perturbation scheme is based on the velocity potential, the amplitude parameter ϵ is most conveniently related to the amplitude of the velocity potential. Accounting for the variation of frequency with amplitude, the expression for φ including all terms through third order is given by:

$$\varphi = \left\{ \epsilon R_n(\alpha) + \epsilon^3 \left[F_5(\alpha) + \zeta_2 \alpha R_n'(\alpha) \right] \right\} \sin(t + n\theta) + \frac{\epsilon^2}{2} \left[R_n^2(\alpha) - (\gamma + 1) f(\alpha) \right] \sin 2(t + n\theta) + \epsilon^3 F_1(\alpha) \sin 3(t + n\theta) \tag{B-29}$$

The parameter ϵ cannot represent the zero-to-peak amplitude of φ since this quantity includes terms proportional to ϵ^2 and ϵ^3. For the same reason ϵ cannot represent the amplitude of the first harmonic term since this quantity includes terms proportional to ϵ^3. A more restrictive definition of ϵ is therefore necessary.

In the analysis to follow, ϵ will be required to represent the amplitude of the term in the velocity potential with the time and space dependence of the first order solution, that is, $R_n(\alpha) \sin(t + n\theta)$. Considering the coefficient of $\sin(t + n\theta)$ in Eq. (B-29), there are three terms: $\epsilon R_n(\alpha)$, $\epsilon^3 F_5(\alpha)$, and $\epsilon^3 \zeta_2 \alpha R_n'(\alpha)$. The last term clearly does not have the same radial dependence as $R_n(\alpha)$ and does not need to be considered further. The term containing $F_5(\alpha)$ needs to be examined further since the homogeneous part of $F_5(\alpha)$ is composed of the same linearly independent functions $J_n(\alpha)$ and $Y_n(\alpha)$ that compose the radial acoustic eigenfunction $R_n(\alpha)$. This occurs because both $F_{5h}(\alpha)$ and $R_n(\alpha)$ are solutions of the same Bessel equation of order n.

The homogeneous part of $F_5(\alpha)$ can therefore be expressed as the sum of two parts, one of which is proportional to $R_n(\alpha)$. Thus $F_{5h}(\alpha)$ can be written as

$$F_{5h}(\alpha) = \left\{ C_{51} - \frac{Y_n(\nu\beta_o)}{J_n(\nu\beta_o)} C_{52} \right\} R_n(\alpha) + Q_n(\alpha) \tag{B-30}$$

where $Q_n(\alpha)$ is a linear combination of $J_n(\alpha)$ and $Y_n(\alpha)$.

Substituting Eq. (B-30) back into Eq. (B-29) yields the following coefficient of the acoustic solution $R_n(\alpha)\sin(t + n\theta)$:

$$A = \epsilon + \epsilon^3 \left[C_{51} - \frac{Y_n(\nu\beta_o)}{J_n(\nu\beta_o)} C_{52} \right] \tag{B-31}$$

Since we desire that the amplitude of the acoustic solution A be equal to the amplitude parameter ϵ, the coefficient of ϵ^3 in Eq. (B-31) must vanish, which gives the following relation between C_{51} and C_{52}:

$$C_{52} = \frac{J_n(\nu\beta_o)}{Y_n(\nu\beta_o)} C_{51} \tag{B-32}$$

This is the additional relationship needed to uniquely determine $F_5(\alpha)$. Equation (B-32) can be substituted into either Eq. (B-22) or Eq. (B-23) to eliminate one of the constants. For instance, substituting Eq. (B-32) into Eq. (B-22) and solving for C_{51} yields

$$C_{51} = \left[\frac{\gamma+1}{4} f'(\nu\beta_o) - \nu\beta_2 \right] \frac{R_n'(\nu\beta_o)}{2J_n(\nu\beta_o)} \qquad \text{(B-33)}$$

For given values of γ, ν, and n, β_2 is first calculated using Eq. (36). Then C_{51} is computed using Eq. (B-33) and is substituted into Eq. (B-32) to determine C_{52}. For a first tangential spinning wave (n=1) and with $\gamma = 1.4$, $\nu = 0.2$ one obtains $\beta_2 = -.49254$, $C_{51} = -0.04460$ and $C_{52} = 0.01861$.

After the constants C_{51} and C_{52} are determined, Eq. (B-18) is used to calculate $F_5(\alpha)$. The functions $I_{51}(\alpha)$ and $I_{52}(\alpha)$ are determined by numerical integration.

In computing the radial velocity by Eq. (43) the derivative $F_5'(\alpha)$ is also needed. Differentiating Eq. (B-18) yields:

$$F_5'(\alpha) = [\, C_{51} - I_{52}(\alpha) \,]\, J_n'(\alpha) + [\, C_{52} + I_{51}(\alpha) \,]\, Y_n'(\alpha)$$

$$- I_{52}'(\alpha) J_n(\alpha) + I_{51}'(\alpha) Y_n(\alpha) \qquad \text{(B-34)}$$

where $I_{51}'(\alpha)$ and $I_{52}'(\alpha)$ are simply the integrands in Eqs. (B-19) and (B-20).

Appendix C.

Third Order Functions for Analysis with Steady Potentials

Using the same techniques employed in Appendix B, the solutions of Eqs. (50) and (51) can be written as the sum of homogeneous and particular solutions as follows:

$$F_4(\alpha) = [C_{41} - 2K_s I_{42}(\alpha)]\, J_n(\alpha) + [C_{42} + 2K_s I_{41}(\alpha)]\, Y_n(\alpha) \tag{C-1}$$

$$F_5(\alpha) = [C_{51} - I_{52}(\alpha) + 2nK_v Q_{52}(\alpha)]\, J_n(\alpha)$$

$$+ [C_{52} + I_{51}(\alpha) - 2nK_v Q_{51}(\alpha)]\, Y_n(\alpha) \tag{C-2}$$

where

$$I_{41}(\alpha) = \int_{\nu\beta_o}^{\alpha} \frac{J_n(x) R_n'(x)}{x W(x)}\, dx \tag{C-3}$$

$$I_{42}(\alpha) = \int_{\nu\beta_o}^{\alpha} \frac{Y_n(x) R_n'(x)}{x W(x)}\, dx \tag{C-4}$$

$$I_{51}(\alpha) = \int_{\nu\beta_o}^{\alpha} \frac{J_n(x) \mathcal{R}_5(x)}{W(x)}\, dx \tag{C-5}$$

$$I_{52}(\alpha) = \int_{\nu\beta_o}^{\alpha} \frac{Y_n(x)\mathcal{R}_5(x)}{W(x)}\,dx \qquad \text{(C-6)}$$

$$Q_{51}(\alpha) = \int_{\nu\beta_o}^{\alpha} \frac{J_n(x)R_n(x)}{x^2W(x)}\,dx \qquad \text{(C-7)}$$

$$Q_{52}(\alpha) = \int_{\nu\beta_o}^{\alpha} \frac{Y_n(x)R_n(x)}{x^2W(x)}\,dx \qquad \text{(C-8)}$$

and $\mathcal{R}_5(\alpha)$ is given by Eq. (B-16) and the Wronskian $W(\alpha)$ is given by

$$W(\alpha) = J_n(\alpha)Y_n'(\alpha) - Y_n(\alpha)J_n'(\alpha) \qquad \text{(C-9)}$$

To complete the solution the constants of integration C_{41}, C_{42}, C_{51}, and C_{52} must be determined.

Applying the boundary conditions on $F_4(\alpha)$ given by Eqs. (57) yields:

$$C_{41}\,J_n(\nu\beta_o) + C_{42}\,Y_n(\nu\beta_o) = \frac{K_s}{\nu\beta_o}\,R_n'(\nu\beta_o) \qquad \text{(C-10)}$$

$$C_{41}\,J_n(\beta_o) + C_{42}\,Y_n(\beta_o) = K_s\left[\frac{1}{\beta_o}\,R_n'(\beta_o) - 2F_{4p}(\beta_o)\right] \qquad \text{(C-11)}$$

where

$$F_{4p}(\beta_o) = I_{41}(\beta_o)Y_n(\beta_o) - I_{42}(\beta_o)J_n(\beta_o) \tag{C-12}$$

while the boundary conditions on $F_5(\alpha)$ given by Eqs. (35) yield:

$$C_{51}J_n(\nu\beta_o) + C_{52}Y_n(\nu\beta_o) = \left[\frac{\gamma+1}{4} f'(\nu\beta_o) - \nu\beta_2\right] R_n'(\nu\beta_o) \tag{C-13}$$

$$C_{51}J_n(\beta_o) + C_{52}Y_n(\beta_o) = \left[\frac{\gamma+1}{4} f'(\beta_o) - \beta_2\right] R_n'(\beta_o) - F_{5p}(\beta_o) + 2nK_vF_{5v}(\beta_o) \tag{C-14}$$

where

$$F_{5p}(\beta_o) = I_{51}(\beta_o)Y_n(\beta_o) - I_{52}(\beta_o)J_n(\beta_o) \tag{C-15}$$

$$F_{5v}(\beta_o) = Q_{51}(\beta_o)Y_n(\beta_o) - Q_{52}(\beta_o)J_n(\beta_o) \tag{C-16}$$

Equations (C-13) and (C-14) contain four unknown quantities: the constants of integration C_{51} and C_{52}, the second order eigenvalue correction β_2, and the vortex constant K_v. As shown in Appendix B the determinant of this system is zero, therefore for solutions to exist the following relation must be satisfied:

$$\frac{\left[\frac{\gamma+1}{4} f'(\nu\beta_o) - \nu\beta_2\right] R_n'(\nu\beta_o)}{\left[\frac{\gamma+1}{4} f'(\beta_o) - \beta_2\right] R_n'(\beta_o) - F_{5p}(\beta_o) + 2nK_v F_{5v}(\beta_o)} = \frac{J_n(\nu\beta_o)}{J_n(\beta_o)} \tag{C-17}$$

Equation (C-17) reduces to Eq. (B-27) for $K_v = 0$. If K_v is known, Equation (C-17) can be used to determine β_2. Using the method of Appendix B where ϵ is required to represent the amplitude of the term in the velocity potential proportional to $R_n(\alpha)\sin(t + n\theta)$, an additional relation between C_{51} and C_{52} is obtained. This relation is the same as Eq. (B-32), that is

$$C_{52} = \frac{J_n(\nu\beta_o)}{Y_n(\nu\beta_o)} C_{51} \tag{C-18}$$

With β_2 and K_v satisfying Eq. (C-17), Eq. (C-18) and either one of Eqs. (C-13) or (C-14) give three equations for the four unknown quantities C_{51}, C_{52}, β_2 and K_v. Thus the boundary conditions do not provide a method of uniquely determining β_2 and $F_5(\alpha)$ when the vortex component of the acoustically driven steady flow is unknown.

Equations (C-10) and (C-11) are two relationships between the unknowns C_{41}, C_{42}, and K_s. The determinant of this system is also zero, and for solutions to exist the following condition must be satisfied:

$$\frac{J_n(\nu\beta_o)}{J_n(\beta_o)} = \frac{R_n'(\nu\beta_o)}{\nu\beta_o} \Bigg/ \left\{ \frac{R_n'(\beta_o)}{\beta_o} - 2F_{4p}(\beta_o) \right\} \tag{C-19}$$

In deriving Eq. (C-19), the steady potential source strength K_s cancels leaving a relationship between fixed quantities which is probably not satisfied. Furthermore, even if Eq. (C-19) is satisfied, the boundary conditions do not provide a means for determining K_s.

C-2

REFERENCES

1. Maslen, S. H., and Moore, F. K., "On Strong Transverse Waves Without Shocks in a Circular Cylinder," Journal of Aeronautical Sciences, Vol. 23, No. 6, 1956, pp. 583-593.

2. Finlayson, B. A., and Scriven, L. E., "The Method of Weighted Residuals--A Review," Applied Mechanics Reviews, Vol. 19, No. 9, September 1966, pp. 735-744.

3. Zinn, B. T. and Powell, E. A., "Nonlinear Combustion Instiability in Liquid Propellant Rocket Engines," Proceedings of the 13th Symposium (International) on Combustion, The Combustion Institute, 1971, pp. 491-503.

4. Padmanabhan, M. S., Powell, E. A., and Zinn, B. T., "Predicting Nonlinear Axial Instabilities in Solid Rockets Using Exact and Approximate Solution Techniques," Proceedings of the 16th Symposium (International) on Combustion, The Combustion Institute, 1977, pp. 1243-1255.

5. Morse, P. M., and Feshbach, H., Methods of Theoretical Physics, McGraw-Hill Book Company, New York 1953, pp. 529-530.